Revista Mexicana de Astronomía y Astrofísica, **59**, 259–277 (2023)

https://doi.org/10.22201/ia.01851101p.2023.59.02.07

MASS PROFILES OF LATE GALAXIES USING A GENETIC ALGORITHM. I - TESTING THE ALGORITHM

Rodolfo de J. Zermeño and Ana M. Hidalgo-Gámez

Escuela Superior de Física y Matemáticas, Instituto Politécnico Nacional, Unidad Profesional Adolfo López Mateos, CDMX, México.

Received March 27 2023; accepted June 8 2023

ABSTRACT

The rotation curve of a galaxy contains a wealth of information about its dynamical properties, being the mass distribution one of the most important. The rotation curve fitting procedures used to estimate the mass profiles of disc galaxies have become more sophisticated over the years, providing ever more reliable results. However, the time-cost and data requirements (e.g. high-resolution NIR photometry) necessary to put to use some of them have restricted these kind of studies to small samples of galaxies. We propose a simple procedure that could be used as a good first approximation for the study of large galaxy samples. It is based on a parameter-fitting method along with a recent optimization algorithm, called the Asexual Genetic Algorithm (AGA). With this procedure, we were able to replicate previously published results, within uncertainties, suggesting that it will provide a reliable first estimation, suitable for its application to large galaxy samples.

RESUMEN

La curva de rotación de una galaxia proporciona vasta información acerca de sus propiedades dinámicas, siendo la distribución de masa una de las más importantes. Los procedimientos de ajuste de curvas de rotación usados para estimar los perfiles de masa en galaxias de disco han mejorado con el tiempo, y han proporcionado resultados cada vez más confiables. Sin embargo, los requisitos en tiempo y calidad de datos (e.g. fotometría NIR de alta resolución) necesarios para poner en uso a algunos de ellos han restringido este tipo de estudios a pequeñas muestras de galaxias. Proponemos un procedimiento simple que podría ser utilizado para obtener una buena primera aproximación en el estudio de grandes muestras. Se basa en un método de ajuste de parámetros en conjunto con un algoritmo genético. Con este procedimiento, fue posible replicar los resultados en la literatura, dentro incertidumbres, lo que sugiere que éste provee una estimación confiable, adecuada para grandes muestras de galaxias.

Key Words: dark matter — galaxies: statistics — galaxies: structure — methods: data analysis

1. INTRODUCTION

The idea of the existence of a halo composed by non-baryonic matter in which the galaxy is completely embedded (Freeman 1970; Rubin et al. 1978; Bosma 1978) was considered after the discovery of an unexpected fast rotation in the outer edges of galaxies, even beyond the optical radius (Bosma 1981; Van Albada & Sancisi 1986). Although over the years alternative models have appeared to explain the rapid rotation of the outer parts of galaxies (Milgrom 1983), the Λ-Cold Dark Matter (hereafter, ΛCDM) paradigm still remains as the most popular, mainly for its simplicity in modelling a great host of phenomena on a vast range of scales (Peebles 2020).

Over the years, several models of dark matter (hereafter, DM) density profiles have been proposed to explain the behavior of the measured rotation curves (hereafter, RCs). Most of the earlier results provided by cosmological DM simulations (Navarro et al. 1997) based on the ΛCDM model predicted a DM density profile with an abrupt rise in density towards the center (i.e., a cusp). However, many studies analyzing RCs from late-type galaxies (mostly Scd - Irr) have systematically found an overestimation of the rotation velocity in the inner regions

when a cusp-type DM density profile is considered (McGaugh et al. 2001; Marchesini et al. 2002; Simon et al. 2005; Kuzio de Naray et al. 2008; Walker & Penarrubia 2011), obtaining better fits with core-type profiles, which show a near constant density at small radius. The disparity between the results of the simulations and the analysis of observed RCs of late galaxies is called the *core-cusp discrepancy* (De Blok 2010).

Such discrepancy, along with the so called disc-halo degeneracy (Carignan & Freeman 1985; van Albada et al. 1985), which describes the situation observed when a certain RC may produce multiple, same-quality, fits (i.e., with comparable χ^2_R) with different stellar disc contributions have encouraged the development of more sophisticated fitting procedures over the years (Blais-Ouellette et al. 2001; Sofue 2012; Katz et al. 2017; Aniyan et al. 2018; Li et al. 2020). However, while all these methods have provided ever more reliable results, the time-cost and data requirements (i.e., high-resolution NIR photometry) needed to implement some of them have restricted these kinds of studies to small samples of galaxies.

With this in mind, we propose a simple procedure based on a parameter fitting method (Sofue 2012, 2013) along with the use of a recent optimization algorithm, called the Asexual Genetic Algorithm (AGA, Cantó et al. 2009). This algorithm has been implemented with success in other studies where a high-accuracy, low-time optimization algorithm was needed, such as orbital parameter fitting from radial velocity data in the search for exoplanets around υ Andromedae (Curiel et al. 2011) and the multi-component analysis of Hα spectra from the jet of the Herbig-Haro object HH34 (Rodríguez-González et al. 2012).

In addition, although some works have explored the influence of using different observational techniques and criteria in the mass profile estimation of disc galaxies (Katz et al. 2017; Korsaga et al. 2019; Li et al. 2020), the influence of some specific aspects of the fitting procedure, such as the chosen optimization algorithm and stellar disc model have not yet been studied in detail. We think that the analysis of RCs extracted from a homogenized data catalog using different fitting procedures [e.g. SPARC database (Lelli et al. 2016b; Li et al. 2020)] is important to find the influence that those considerations might have over the resulting fits, such as possible systematic effects visible through a direct comparison between them. For this reason, we think that this simple approach might prove to be really useful, serving also as a complement to previous studies.

The main goal of this manuscript is twofold: First, to check the reliability of our procedure. In order to achieve this we analyze a set of RC data extracted from the SPARC database (Lelli et al. 2016b), and then compare our results to those available in the literature (Li et al. 2020), previously obtained through a different procedure on the same dataset (i.e. SPARC). And second, to search for any systematic effects that could be attributed to a difference between procedures. Therefore, proving our procedure to be reliable, i.e. finding that our results do not deviate significantly from the ones already published, would imply that:

- The optimization algorithm (AGA) does a competent job providing a simple, low time-cost method to fit kinematical data for the mass profile estimation of late galaxies. Moreover, it does not require high spatial resolution photometry (which is not always available) to provide reliable results. These latter characteristics would make it suitable for analyzing samples with a great number of galaxies, using photometry data from widely available standardized digital surveys [e.g. SDSS (Abdurro'uf et al. 2022)].

- Would reinforce the argument that the use of an homogenized RC database serves as one of the most important factors in reducing the scatter between results (Li et al. 2020), limiting the influence of the assumed stellar disc models and optimization algorithms.

On the contrary, if the results obtained here show a systematic difference from those already published, independently of the assumed DM density profiles, it might be concluded that our assumed optimization algorithm and set of constraints show a bias, or that the simple stellar disc model assumed in this work is not a good approximation for practical purposes.

The present work comprises seven sections: in § 2, we make a brief description of the optimization algorithm, the Asexual Genetic Algorithm (AGA), and some of its characteristics. § 3 describes the test sample along with its selection criteria. In § 4 we detail the adopted mass models for each component, information about the photometry and M/L used as constraints in the fitting procedure, along with a description on how the fitting procedure was implemented. Finally, § 5 and 6 contain our results and conclusions, respectively.

2. ASEXUAL GENETIC ALGORITHM (AGA)

AGA is an optimization algorithm based on the selection of the fittest *individuals* (points in a N-dimensional space of parameters) through successive generations until convergence is achieved. These individuals are evaluated with the theoretical model and then compared with the observational data using a previously established *survival criterion*, a function (e.g. the reduced χ^2 function,

χ^2_R) whose value determines if the evaluated point is conserved for the next generation. A detailed description of this function is given in § 4.4.

According to the AGA main paper (Cantó et al. 2009), the most important difference between AGA and other 'standard' genetic algorithms (Holland et al. 1992) lies in the way the new generations are constructed. Standard genetic algorithms involve *sexual reproduction*, which involves the union of 'male' and 'female' reproductive individuals. Instead, AGA uses *asexual reproduction with mutation*, where a single individual can produce offspring by generating a random point within a narrow neighborhood around it. The size of this neighborhood can be specified by the user to reduce convergence time (Rodríguez-González et al. 2012). It is important to note that every new generation a clone of the parent individual is always conserved in case their offspring is less suited. When the first guess is far from the solution, AGA is capable of *migrating* the search to the optimal true solution. The optimal solution is normally obtained after a few hundred iterations. The combination of these characteristics makes AGA a reliable and fast-converging optimization algorithm, suitable for problems with many local minima/maxima close to the true solution.

3. TEST SAMPLE

Our test sample consists of 100 late-type galaxies selected from the *Spitzer Photometry and Accurate Rotation Curves* (SPARC) database (Lelli et al. 2016b). This catalog contains kinematical data (hybrid Hα+HI RCs) for 175 late-type galaxies along with their near-infrared (NIR) Spitzer 3.6μm photometry. Additionally, it contains a set of disk mass models calculated using the Casertano formula (Casertano 1983), a solution of the Poisson equation considering a finite thickness disc with an arbitrary radial density distribution. Since all the RCs in the SPARC catalog have been treated in a homogeneous manner, it provides the community with a *standardized* data sample, which works as an ideal reference to study the influence of the adopted fitting procedure in the mass estimation problem. The complete list of galaxies considered in the present work is condensed in Table 1 along with their most important characteristics. To simplify our analysis, as a first implementation of our procedure we selected galaxies that are classified in the SPARC database as lacking a bulge component, considering only the stellar disk, HI disk and dark matter halo. Since we are considering the same components as the ones assumed for the extraction of the published fits, this will allow us to make a reliable comparison between results.

4. FITTING PROCEDURE

In this section we detail the chosen disc and dark matter halo mass models as well as the main characteristics of our fitting procedure. We also include a subsection which describes briefly how the optimization algorithm was implemented, along with the method used to estimate the uncertainty of our results.

4.1. *Disc and Halo Models*

In this work, we use the method described by Sofue (2012), where the total rotation velocity at radius R is defined as:

$$V_t^2 = V_b^2 + V_d^2 + V_h^2 + V_{HI}^2, \tag{1}$$

where V_t is the total rotation velocity and V_b,V_d,V_h,V_{HI} are the rotation velocity components for the bulge, disc, DM halo and HI disc, respectively. For the present study, since our sample is composed of late spiral and irregular galaxies, we will consider the velocity contribution of a bulge component as negligible.

The stellar disc velocity component, V_d, was determined with the analytical expression obtained from the Poisson equation for a thin disc following an exponential surface density profile and a constant M/L along the radius (Freeman 1970; Binney & Tremaine 1987).

$$V_d\,(R) = \sqrt{\frac{GM_d}{a_d}}\,D\,(X)\,, \tag{2}$$

where M_d is the total stellar disc mass, a_d the exponential scale radius and $D\,(X)$ is defined as:

$$D\,(X) = \left(\frac{X}{\sqrt{2}}\right)\left[I_0\left(\frac{X}{2}\right)K_0\left(\frac{X}{2}\right) - I_1\left(\frac{X}{2}\right)K_1\left(\frac{X}{2}\right)\right]^{1/2}, \tag{3}$$

being I_i y K_i the modified Bessel functions and $X = \frac{R}{a_d}$. The two free parameters are the total stellar disc mass, M_d, and the exponential scale radius, a_d. In the present investigation, the DM halo was modelled assuming three different density profiles: Navarro-Frenk-White (hereafter, NFW) (Navarro et al. 1997), pseudo-isothermal (ISO) (Kent 1986), and Burkert-type (BURK) (Burkert 1995). They are described as:

$$\rho_h^{NFW}\,(R) = \frac{\rho_0}{\frac{R}{h}\left(1+\frac{R}{h}\right)^2}; \tag{4}$$

$$\rho_h^{ISO}\,(R) = \frac{\rho_0}{\left(1+\left(\frac{R}{h}\right)^2\right)}; \tag{5}$$

$$\rho_h^{BURK}\,(R) = \frac{\rho_0}{\left(1+\frac{R}{h}\right)\left(1+\left(\frac{R}{h}\right)^2\right)}, \tag{6}$$

where ρ_0 is the *core density* and h is the *scale length* of the DM halo. Considering spherical symmetry, the total halo mass is obtained by integrating along the radius, giving

TABLE 1

MAIN PROPERTIES OF SPARC TEST SAMPLE[a]

Name	Hubble Type	D (Mpc)	i (°)	L (3.6 μm) ($10^{10} L_\odot$)	a_d (pc)	μ_0 ($L_\odot$/pc^2)	HI total mass ($10^{10} M_\odot$)
D512-2	Im	15.2 ± 4.56	56 ± 10	0.0325 ± 0.0022	1240	93.94	0.0081
D564-8	Im	8.79 ± 0.28	63 ± 7	0.0033 ± 0.0004	610	21.13	0.0029
D631-7	Im	7.72 ± 0.18	59 ± 3	0.0196 ± 0.0009	700	115.04	0.029
DDO064	Im	6.8 ± 2.04	60 ± 5	0.0157 ± 0.0007	690	151.65	0.0211
DDO154	Im	4.04 ± 0.2	64 ± 3	0.0053 ± 0.0002	370	71.26	0.0275
DDO161	Im	7.5 ± 2.25	70 ± 10	0.0548 ± 0.0015	1220	169.37	0.1378
DDO168	Im	4.25 ± 0.21	63 ± 6	0.0191 ± 0.0005	1020	92.22	0.0413
DDO170	Im	15.4 ± 4.62	66 ± 7	0.0543 ± 0.003	1950	73.93	0.0735
ESO079-G014	Sbc	28.7 ± 7.17	79 ± 5	5.17 ± 0.05	5080	2295.25	0.314
ESO116-G012	Sd	13 ± 3.9	74 ± 3	0.4292 ± 0.007	1510	1320.78	0.1083
ESO444-G084	Im	4.83 ± 0.48	32 ± 6	0.007 ± 0.0003	460	66.81	0.0135
ESO563-G021	Sbc	60.8 ± 9.1	83 ± 3	31.12 ± 0.26	5450	6558.89	2.4298
F563-1	Sm	48.9 ± 9.8	25 ± 5	0.19 ± 0.02	3520	41.77	0.32
F563-V1	Im	54 ± 10.8	60 ± 10	0.15 ± 0.017	3790	40.63	0.061
F563-V2	Im	59.7 ± 11.9	29 ± 10	0.2986 ± 0.0267	2430	146.16	0.2169
F565-V2	Im	51.8 ± 10.4	60 ± 10	0.06 ± 0.01	2170	40.26	0.0699
F567-2	Sm	79 ± 11.8	20 ± 10	0.2134 ± 0.0305	3080	46.65	0.2449
F568-1	Sc	90.7 ± 9.7	26 ± 5	0.6252 ± 0.0564	5180	57.13	0.4498
F568-3	Sd	82.4 ± 8.24	40 ± 10	0.8346 ± 0.0592	4990	132.08	0.3195
F568-V1	Sd	80.6 ± 8.06	40 ± 10	0.3825 ± 0.0384	2850	90.54	0.2491
F571-8	Sc	53.3 ± 10.7	85 ± 5	1.0164 ± 0.0412	3560	87.26	0.1782
F571-V1	Sd	80.1 ± 8	30 ± 10	0.1849 ± 0.0267	2470	64.39	0.1217
F574-1	Sd	96.8 ± 9.68	65 ± 10	0.6537 ± 0.0596	4460	128.48	0.3524
F574-2	Sm	89.1 ± 8.91	30 ± 10	0.2877 ± 0.0384	3760	41.38	0.1701
F579-V1	Sc	89.5 ± 8.95	26 ± 10	1.1848 ± 0.0742	3370	201.76	0.2245
F583-1	Sm	35.4 ± 8.85	63 ± 5	0.0986 ± 0.0093	2360	60.93	0.2126
F583-4	Sc	53.3 ± 10.7	55 ± 10	0.1715 ± 0.0185	1930	83.34	0.0641
IC2574	Sm	3.91 ± 0.2	75 ± 7	0.1016 ± 0.0012	2780	80.32	0.1036
KK98-251	Im	6.8 ± 2.04	59 ± 5	0.0085 ± 0.0007	1340	52.1	0.0115
NGC0024	Sc	7.3 ± 0.36	64 ± 3	0.3889 ± 0.0036	1340	1182.58	0.0676
NGC0055	Sm	2.11 ± 0.11	77 ± 3	0.4628 ± 0.0013	6110	391.59	0.1565
NGC0247	Sd	3.7 ± 0.19	74 ± 3	0.7332 ± 0.0027	3740	506.79	0.1746
NGC1003	Scd	11.4 ± 3.42	67 ± 5	0.682 ± 0.0075	1610	1345.33	0.588
NGC2403	Scd	3.16 ± 0.16	63 ± 3	1.0041 ± 0.0028	1390	1408.74	0.3199
NGC3109	Sm	1.33 ± 0.07	70 ± 5	0.0194 ± 0.0002	1560	140.87	0.0477
NGC3198	Sc	13.8 ± 1.4	73 ± 3	3.8279 ± 0.0212	3140	1602.62	1.0869
NGC3741	Im	3.21 ± 0.17	70 ± 4	0.0028 ± 0.0001	200	143.49	0.0182
NGC3769	Sb	18 ± 2.5	70 ± 2	1.8679 ± 0.0189	3380	160.26	0.5529
NGC3893	Sc	18 ± 2.5	49 ± 2	5.8525 ± 0.0377	2380	2055.09	0.5799
NGC3917	Scd	18 ± 2.5	79 ± 2	2.1966 ± 0.0202	2630	1226.96	0.1888
NGC3992	Sbc	23.7 ± 2.3	56 ± 2	22.6932 ± 0.0836	4960	3257.09	1.6599
NGC4010	Sd	18 ± 2.5	89 ± 1	1.7193 ± 0.019	2810	2611.14	0.2832
NGC4100	Sbc	18 ± 2.5	73 ± 2	5.9394 ± 0.0328	2150	8970.78	0.3102
NGC4183	Scd	18 ± 2.5	82 ± 2	1.084 ± 0.015	2790	1098.58	0.3506
NGC4559	Scd	9 ± 2.7	67 ± 1	1.9377 ± 0.0107	2100	1602.62	0.5811
NGC5585	Sd	7.06 ± 2.12	51 ± 2	0.2943 ± 0.0033	1530	297.05	0.1683
NGC6015	Scd	17 ± 5.1	60 ± 2	3.2129 ± 0.0237	2300	1926.77	0.5834
NGC7793	Sd	3.61 ± 0.18	47 ± 9	0.705 ± 0.0026	1210	1068.64	0.0861
UGC00128	Sdm	64.5 ± 9.7	57 ± 10	1.2 ± 0.06	5950	88.89	0.7431
UGC00191	Sm	17.1 ± 5.1	45 ± 5	0.2004 ± 0.0063	1580	207.41	0.1343

TABLE 1. CONTINUED

Name	Hubble Type	D (Mpc)	i (°)	L (3.6 μm) ($10^{10} L_\odot$)	a_d (pc)	μ_0 ($L_\odot/pc^2$)	HI total mass ($10^{10} M_\odot$)
UGC00634	Sm	30.9 ± 7.7	37 ± 8	0.2989 ± 0.0146	2450	126.13	0.3663
UGC00731	Im	12.5 ± 3.75	57 ± 3	0.0323 ± 0.0019	2300	82.57	0.1807
UGC00891	Sm	10.2 ± 3.1	60 ± 5	0.0374 ± 0.0017	1430	113.98	0.0428
UGC01230	Sm	53.7 ± 10.7	22 ± 10	0.762 ± 0.0379	4340	69.32	0.643
UGC02259	Sdm	10.5 ± 3.1	41 ± 3	0.1725 ± 0.0038	1620	172.52	0.0494
UGC04325	Sm	9.6 ± 2.88	41 ± 3	0.2026 ± 0.0035	1860	213.22	0.0678
UGC04483	Im	3.34 ± 0.31	58 ± 3	0.0013 ± 0.0001	180	82.57	0.0032
UGC04499	Sdm	12.5 ± 3.75	50 ± 3	0.1552 ± 0.0043	1730	127.3	0.11
UGC05005	Im	53.7 ± 10.7	41 ± 10	0.41 ± 0.0283	3200	65.59	0.3093
UGC05414	Im	9.4 ± 2.82	55 ± 3	0.1123 ± 0.0028	1470	127.3	0.0574
UGC05716	Sm	21.3 ± 5.3	54 ± 10	0.0588 ± 0.0042	1140	90.54	0.1094
UGC05721	Sd	6.18 ± 1.85	61 ± 5	0.0531 ± 0.0011	380	913.76	0.0562
UGC05750	Sdm	58.7 ± 11.7	64 ± 10	0.3336 ± 0.0264	3460	124.98	0.1099
UGC05764	Im	7.47 ± 2.24	60 ± 10	0.0085 ± 0.0006	1170	33.79	0.0163
UGC05829	Im	8.64 ± 2.59	34 ± 10	0.0564 ± 0.0019	1990	63.22	0.1023
UGC05918	Im	7.66 ± 2.3	46 ± 5	0.0233 ± 0.0011	1660	24.94	0.0297
UGC05986	Sm	8.63 ± 2.59	90 ± 3	0.4695 ± 0.0048	1670	1725.16	0.2667
UGC05999	Im	47.7 ± 9.5	22 ± 10	0.3384 ± 0.0231	3220	51.62	0.2022
UGC06399	Sm	18 ± 2.5	75 ± 2	0.2296 ± 0.0072	2050	311.05	0.0674
UGC06446	Sd	12 ± 3.6	51 ± 3	0.0988 ± 0.0032	1490	86.46	0.1379
UGC06667	Scd	18 ± 2.5	89 ± 1	0.1397 ± 0.0066	5150	614.94	0.0809
UGC06917	Sm	18 ± 2.5	56 ± 2	0.6832 ± 0.012	2760	261.11	0.2023
UGC06923	Im	18 ± 2.5	65 ± 2	0.289 ± 0.0077	1440	347.4	0.0809
UGC06930	Sd	18 ± 2.5	32 ± 5	0.8932 ± 0.014	3940	189.16	0.3237
UGC06983	Scd	18 ± 2.5	49 ± 1	0.5298 ± 0.0102	3210	121.57	0.2967
UGC07089	Sdm	18 ± 2.5	80 ± 3	0.3585 ± 0.0089	2260	520.99	0.1214
UGC07125	Sm	19.8 ± 5.9	90 ± 3	0.2712 ± 0.008	3380	103	0.4629
UGC07151	Scd	6.87 ± 0.34	90 ± 3	0.2284 ± 0.0025	1250	965.67	0.0616
UGC07261	Sdm	13.1 ± 3.93	30 ± 10	0.1753 ± 0.0048	1200	566.02	0.1388
UGC07399	Sdm	8.43 ± 2.53	55 ± 3	0.1156 ± 0.0024	1640	135.78	0.0745
UGC07524	Sm	4.74 ± 0.24	46 ± 3	0.2436 ± 0.0025	3460	106.86	0.1779
UGC07559	Im	4.97 ± 0.25	61 ± 3	0.0109 ± 0.0004	580	55.06	0.0169
UGC07603	Sd	4.7 ± 1.41	78 ± 3	0.0376 ± 0.0008	530	520.99	0.0258
UGC07608	Im	8.21 ± 2.46	25 ± 10	0.0264 ± 0.0012	1500	46.65	0.0535
UGC07690	Im	8.11 ± 2.43	41 ± 5	0.0858 ± 0.0018	570	395.21	0.039
UGC07866	Im	4.57 ± 0.23	44 ± 5	0.0124 ± 0.0004	610	97.46	0.0118
UGC08286	Scd	6.5 ± 0.21	90 ± 3	0.1255 ± 0.0018	1050	1488.78	0.0642
UGC08490	Sm	4.65 ± 0.53	50 ± 3	0.1017 ± 0.0012	670	576.54	0.072
UGC08550	Sd	6.7 ± 2	90 ± 3	0.0289 ± 0.0009	450	1284.78	0.0288
UGC09037	Scd	83.6 ± 8.4	65 ± 5	6.8614 ± 0.1769	4280	841.07	1.9078
UGC10310	Sm	15.2 ± 4.6	34 ± 6	0.1741 ± 0.0053	1800	158.79	0.1196
UGC11455	Scd	78.6 ± 11.8	90 ± 1	37.4322 ± 0.3792	5930	9568.2	1.3335
UGC11557	Sdm	24.2 ± 6.05	30 ± 10	1.2101 ± 0.0212	2750	337.93	0.2605
UGC11820	Sm	18.1 ± 5.43	45 ± 10	0.097 ± 0.0047	2080	34.11	0.1977
UGC12506	Scd	100.6 ± 10.1	86 ± 4	13.9571 ± 0.3214	7380	5608.28	3.5556
UGC12632	Sm	9.77 ± 2.93	46 ± 3	0.1301 ± 0.003	2420	66.81	0.1744
UGC12732	Sm	13.2 ± 4	39 ± 6	0.1667 ± 0.0048	1980	120.46	0.366
UGCA281	BCD	5.68 ± 0.28	67 ± 3	0.0194 ± 0.0007	1720	12.05	0.0062
UGCA442	Sm	4.35 ± 0.22	64 ± 7	0.014 ± 0.0005	1180	116.1	0.0263
UGCA444	Im	0.98 ± 0.05	78 ± 4	0.0012 ± 0	830	22.74	0.0067

[a]Properties of selected SPARC test sample. The galaxy name is given in the first Column while the morphological type, according to SPARC, is shown in the second Column. The distance and inclination are shown in Columns 3 and 4, while the 3.6 μm luminosity is tabulated in Column 5. Finally, the exponential scale radius (a_d), the central surface brightness (μ_0) and the estimated HI total mass are listed in Columns 6, 7 and 8, respectively.Data extracted from the SPARC database website (Lelli et al. 2016b).

the following expressions for the NFW, ISO and BURK profiles, respectively:

$$M_h^{NFW}(R) = 4\pi\rho_0 h^3 \left\{ \ln\left(1+\frac{R}{h}\right) - \frac{\frac{R}{h}}{1+\frac{R}{h}} \right\}; \quad (7)$$

$$M_h^{ISO}(R) = 4\pi\rho_0 h^2 \left\{ R - h\arctan\left(\frac{R}{h}\right) \right\}; \quad (8)$$

$$M_h^{B}(R) = 4\pi\rho_0 h^3 \left\{ \ln\frac{\sqrt{h+R}(R^2+h^2)^{1/4}}{h} - \frac{1}{2}\arctan\left(\frac{R}{h}\right) \right\}. \quad (9)$$

The rotation velocity component for the dark matter halo at radius R is:

$$V_h(R) = \sqrt{\frac{GM_h}{R}}. \quad (10)$$

DM density profiles are often expressed in terms of the rotation velocity at the virial radius, V_{200}, and the concentration parameter, c, defined as:

$$V_{200} = \sqrt{\frac{GM_{200}}{R_{200}}}; \quad (11)$$

$$c = \frac{R_{200}}{h}, \quad (12)$$

where R_{200} is the radius of a spherical halo with a mass equal to M_{200} and the virial mass M_{200} is defined as the total mass contained within a sphere whose *mean* density equals 200 times the critical density of the Universe (ρ_c) at $z = 0$

$$M_{200} = \frac{4}{3}\pi R_{200}^3 (200\rho_c). \quad (13)$$

We have considered a Hubble constant value of $H_0 = 73\,km\,s^{-1}Mpc^{-1}$ (Riess et al. 2022) throughout this investigation. This value is the same as the one assumed in the published fits used as comparison (Li et al. 2020).

4.2. *HI Disc Velocity Component*

Since all the elements in our sample are classified as late-type galaxies (mostly Sm and Irr), it should be necessary to take into account the dynamical effects of a separate HI disc component because such galaxies tend to have an important fraction of their total baryonic mass in the form of HI (Roberts 1962; Huchtmeier & Richter 1989; Korsaga et al. 2019). In this work, the HI disc velocity component is obtained from the SPARC database HI mass model for each galaxy. This component is calculated with the Casertano (1983) formula. In this investigation, in order to isolate the contributions of the stellar disc and DM halo, the HI disc velocity component for each point in the RC is subtracted from the observed rotation velocity using the following expression:

$$V_{corr}(R) = \sqrt{V_{obs}^2 - V_{HI}^2}, \quad (14)$$

where V_{obs} is the observed rotation velocity , V_{HI} the HI disc velocity component and V_{corr} the *corrected velocity*. This latter component is then inserted in the fitting algorithm and analysed.

4.3. *Photometry and* $(M/L)_\star$ *Ratio*

In all the problems that involve the fitting of observational data using a certain theoretical model it is important to select a suitable set of constraints to ensure that our algorithm does not give unrealistic results. One important constraint in RC analysis is the surface brightness photometry (Katz et al. 2017; Korsaga et al. 2019; Li et al. 2020). The surface brightness profile of the galaxy provides information about how the stars are distributed throughout the disc. In recent years, many studies have shown that near-infrared (NIR) surface photometry can be used as an excellent stellar disc mass tracer, since these bands are less susceptible to systematic uncertainties caused by dust emission that afflict the optical bands (Kennicutt et al. 2003; Leroy et al. 2008; Meidt et al. 2014). Another reason is that most of the stellar disc total mass is composed of low-mass stars, whose main emission is at NIR bands (Kroupa & Jerabkova 2021). This is seen as a low dispersion on the (M/L)-color correlation at NIR bands compared to the optical bands (Bell & de Jong 2001). In this work, we used the exponential disc scale length (a_d) and the 3.6 μm total luminosity ($L_T^{3.6\mu m}$), extracted from the SPARC database (Table 1). It is important to note that, although the thin disk model (Freeman 1970; Binney & Tremaine 1987) represents a simplification with respect to models used in other studies, it has the advantage of only depending on two photometric parameters (L_T, a_d) to estimate the stellar disk contribution, instead of requiring a complete luminosity profile obtained with high spatial resolution observations (Casertano 1983). In the case of low-mass galaxies, the exponential profile is usually a good approximation for a large interval of radii (Lelli et al. 2016b). However, it is common to find small deviations on the disc caused by secondary structures, such as bars or spiral arms.

Another important constraint in our model is the $(M/L)_\star$ ratio for the stellar disc. As mentioned in the Introduction, the uncertainty in this parameter is mainly responsible for the disc-halo degeneracy. A way to counter this degeneracy is by considering the *maximal disc hypothesis*, where the contribution of the disc mass to the RC is considered to be as large as the RC itself allows it. Qualitatively, it is defined as a disc whose contribution

to the total potential exceeds the contribution of the dark matter halo in the inner regions. However, in recent years evidence was found suggesting that the application of the maximum disc hypothesis usually resulted in $(M/L)_\star$ values that were too high compared to those predicted by the stellar population synthesis (SPS) models (McGaugh & Schombert 2014; Schombert & McGaugh 2014). This effect is more noticeable in late type galaxies (Sc, Sd, Irr), where the contribution of a bulge is small or nonexistent. Thus, when a plausible range for $(M/L)_\star$ is considered, the resulting fits show DM halos whose contributions to the total rotation velocity are dominant at all radii. The discs that show this property are classified as *submaximal* (Sackett 1997).

For this first implementation and testing of our procedure, we decided to fix the $(M/L)_\star$ ratio instead of considering it as a free parameter. This was done in order to avoid adding another free parameter to the algorithm, hampering the interpretation of our results. We fixed this ratio at $(M/L)_\star = 0.5$, constant along the disc, which many studies have converged to take as the fiducial value at 3.6 μm (McGaugh & Schombert 2014; Schombert & McGaugh 2014; Lelli et al. 2016a), consistent with the results of stellar population synthesis (SPS) models (Bruzual & Charlot 2003; Meidt et al. 2014).

4.4. *AGA Selection Criterion, the χ^2_R Function*

As we briefly mentioned in the Introduction, in the present work we use the χ^2_R function as the selection criterion for AGA, which is defined as:

$$\chi^2_R = \frac{1}{N-P}\sum_{i=1}^{N}\frac{\left(V_i^{obs}-V_i^t\right)^2}{\sigma_i^2}; \qquad (15)$$

where N is the number of RC data points, P the number of free parameters, V_i^{obs} the observed rotation velocity, V_i^t the calculated total rotation velocity and σ_i the observational uncertainties. After establishing the photometry constraints, the remaining free parameters are the ones corresponding to the DM halo (ρ_0 and h), thus $P = 2$.

4.5. *Uncertainty Estimation*

In order to estimate the uncertainty range of our results, we use the methodology described in the AGA main paper (Cantó et al. 2009), based in the generation of *synthetic data sets*. The process is quite simple: for each data point of the measured curve, a random data point is generated inside the observational velocity uncertainty interval 2σ. The procedure is repeated until a set of synthetic RCs is obtained. These synthetic curves serve as *statistical equivalents* on the uncertainty estimation. Each one is treated and analysed in the same way as the measured RCs. The formula used for the generation of synthetic RCs is:

$$V'(R) = V_{obs}(R) + \sigma(2\xi - 1), \qquad (16)$$

where $V'(R)$ is the synthetic rotation velocity value, $V_{obs}(R)$ the measured rotation velocity, σ the observational error and ξ is a random variable in the interval $[0, 1]$. In the present work, the uncertainties were estimated using sets with an average of 6 synthetic RCs per galaxy. This number was chosen after some tests designed to find the best compromise between time and accuracy. The uncertainties are defined as the standard deviation of the parameter distribution for the synthetic data set.

4.6. *Python Subroutine*

Adapting AGA to our procedure required to implement some modifications in the code. As mentioned in section 4, the stellar disc contribution is calculated from equation (2), which contains the first and second order modified Bessel functions. The language in which AGA is compiled (FORTRAN90) does not support these functions implicitly, so it was necessary to add them as an external module. These functions were adapted from the FORTRAN special function package, SPECFUN (Cody 1993). Individual tests were performed for each function to ensure they worked correctly.

The fitting procedure was compiled as a Python subroutine, whose main purpose was to provide AGA with all the information needed from a set of machine-readable tables containing the SPARC data for each galaxy in the sample. These data consisted of the measured RC, the disc exponential scale length (a_d), the galaxy total luminosity at 3.6 μm ($L_\odot^{3.6\mu m}$) and the HI velocity component. Once a fit was obtained for the specified RC, the subroutine then estimated the corresponding c, V_{200}, M_{200} and R_{200} values by using the numerical solver included in the SYMPY package (Meurer et al. 2017). In order to guarantee a good coverage of the parameter space, we established a set of loose constraints for our fitting variables. In the case of the DM profile core density, ρ_0, we set a range between $0 \leq \rho_0 \leq 1\ M_\odot\ \mathrm{pc}^{-3}$, while the scale parameter h could vary between $0 \leq h \leq 100$ kpc. The typical values of ρ_0 and h tend to be of the order of $\rho_0 \approx 10^{-2} M_\odot\ \mathrm{pc}^{-3}$ and $h \approx 10^3 - 10^4$ pc (Sofue 2012, 2013).

Each AGA run consisted of 150 generations, containing 1000 individual points in the parameter space (200 *parent* + 800 *offspring*), with a *box size* factor of 0.5 between generations. The box size factor reduces the parameter-space volume from which new points can be generated around each individual between one generation and the next. Every AGA run starts with a box size spanning the full specified parameter range. The result is then stored and used as a starting point for the next run. This procedure may seem redundant at first, but it is important to note that for each run, the sizes of the sampling boxes

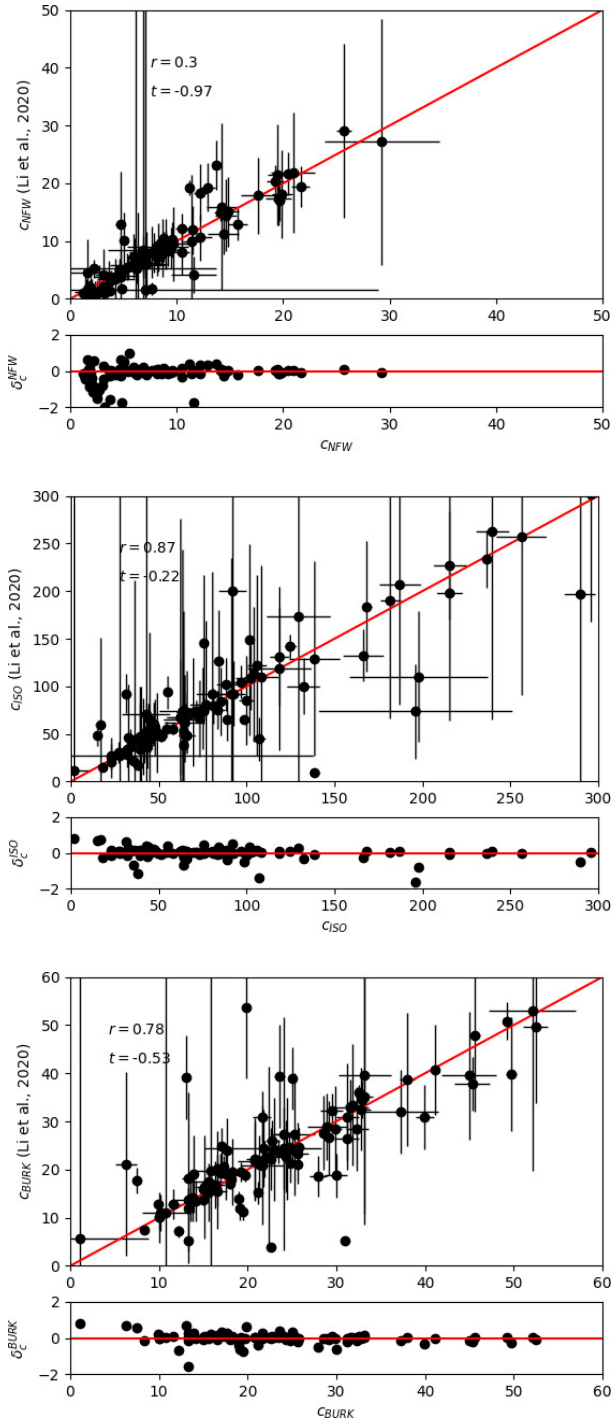

Fig. 1. Comparison diagrams of the best-fit c values obtained with our procedure against their corresponding published fits in the SPARC database (Li et al. 2020). The $y = x$ line is indicated in red. The corresponding residual graphs, described in terms of the deviation parameter δ_c (Equation 17) are located below each comparison diagram. On all DM profiles, most galaxies in our sample ($\gtrsim 90\%$) lie within $\delta_c \leq 1$. The color figure can be viewed online.

are reset to their initial values, so each run starts searching for the solution using boxes of the same size as the ones used in the first run, but centered on improved initial values (Cantó et al. 2009). This enhances the accuracy of the algorithm and reduces the probability of converging on a local minimum. Finally, after 6 consecutive runs, the results are stored as the best-fit parameters.

5. RESULTS

Tables A1, A2 and A3 (Appendix A) list the obtained best-fit c, M_{200}, R_{200}, V_{200} and χ^2_R values for all the galaxies in this sample, assuming a NFW, ISO and BURK DM halo profiles, respectively. In the present work, for the comparison between obtained and published fits we will focus on two independent parameters: the concentration parameter, c, and the virial rotation velocity, V_{200}. As explained in § 4.1, the DM profile can be completely characterized by these two parameters.

In the analyzed sample, the typical values found for the concentration parameter c depend on the assumed DM profile. For example, for a NFW profile, the typical values are around $c_{NFW} \approx 10 - 20$, while for ISO and BURK, the typical values are around $c_{ISO} \approx 80$ and $c_{BURK} \approx 20 - 30$. In the case of the parameter V_{200}, for all DM profiles, the typical values are around $V_{200} \approx 100\,\mathrm{km\,s^{-1}}$. It can be seen from Tables A1, A2 and A3 that only a handful of galaxies show values far-off from the average ones for c or V_{200}, being the BURK profile the one with the least number of outlying galaxies (only two of them) while the ISO profile shows the largest number of outliers.

5.1. *Comparison with Previous Results*

Figures 1 and 2 compare our obtained best-fit parameter values against their corresponding values found in the literature (Li et al. 2020) assuming each DM density profile for the parameters c and V_{200}, respectively. A qualitative analysis shows that most galaxies in these diagrams lie near the red $y = x$ line, within uncertainties, implying a great degree of consistency between studies. However, some deviations were found (e.g. Figure 2, top), which will be addressed below.

In order to verify in a quantitative manner if our results are consistent with those found in the literature, we compared our obtained best-fit c and V_{200} samples against their corresponding published values through a set of paired t-tests. According to these tests, for a sample size of 100 galaxies with a 95% confidence level, the critical t value, T (from which we can reject the same-mean hypothesis) is equal to 1.98. If the absolute values of t_c or $t_{V_{200}}$ are higher than T, we can consider that the difference between the means of our compared samples is statistically significant. The t-test results, along with their corresponding Pearson correlation values for the parameters c (r_c) and V_{200} ($r_{V_{200}}$) are condensed in Table 2.

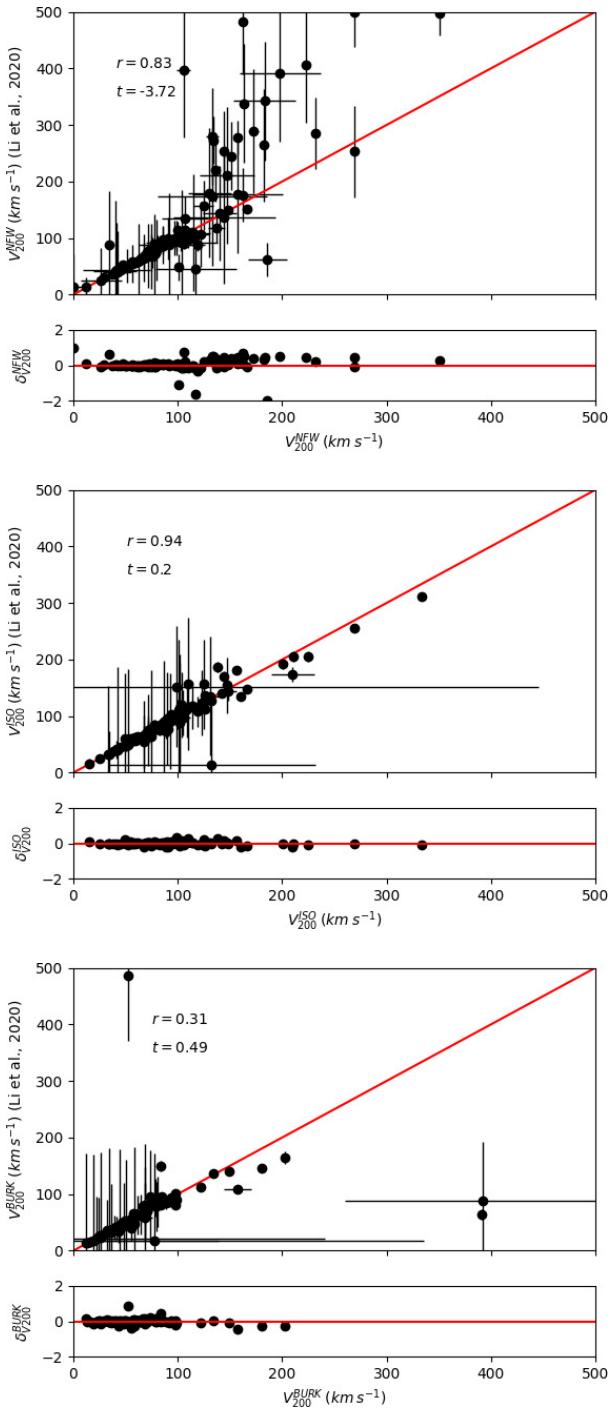

Fig. 2. Comparison diagrams of the best-fit V_{200} values obtained with our procedure against their corresponding published fits in the SPARC database (Li et al. 2020). The $y = x$ line is indicated in red. The corresponding residual graphs, described in terms of the deviation parameter δ_{V200} (equation 18) are located below each comparison diagram. On all DM profiles, most galaxies in our sample ($\gtrsim$ 90%) lie within $\delta_{V200} \leq 1$. The color figure can be viewed online.

The t-test analysis shows that our fits pass the equal-mean hypothesis in 5 out of the 6 possible tests (2 fit parameters, 3 DM profiles). The only t-test that did not pass corresponds to the comparison between our obtained vs the published V_{200}^{NFW} samples. This is seen in the V_{200}^{NFW} comparison diagram (Figure 2, top) as a divergence from the $y = x$ line at $V_{200}^{NFW} \gtrsim 200$ km s^{-1} . It is interesting to note that most of the galaxies that deviate from the $y = x$ line show h values that lie near the upper limit imposed for our procedure ($h \approx 100$ kpc), indicating that the global minimum probably did not fall inside our specified h range. In order to explore this, several runs were performed assuming different upper range values for h. We found that, although the χ^2_R global minimum was reached, the resulting parameter values would not be physical (i.e. $V_{200} > 500$ km s^{-1}) (Li et al. 2020). This behaviour was found exclusively when a NFW profile was considered.

Along with the t-tests, to quantify the deviation between the obtained and the published parameter values for each individual galaxy, we define a *deviation parameter* (δ_c and $\delta_{V_{200}}$ for c and V_{200}, respectively) by using the following expressions:

$$\delta_c = 1 - \frac{c}{c^{bib}}, \tag{17}$$

$$\delta_{V_{200}} = 1 - \frac{V_{200}}{V_{200}^{bib}}, \tag{18}$$

where c^{bib} and V_{200}^{bib} are the published c and V_{200} values from SPARC, respectively. The number of galaxies in our sample with δ_c and $\delta_{V_{200}}$ below different thresholds is described in Table 3.

Table 3 shows that in the case of the ISO and BURK profiles the fraction of galaxies in our sample with $|\delta_c|, |\delta_{V_{200}}| \leq 1$ is 95% and 94%, respectively, while the NFW profile only reached 85%. These results indicate that the core-type profiles, such as ISO and BURK, are closer to the respective published values than those obtained assuming a NFW profile.

Regarding the Pearson correlation (r_c, r_{V200}) between datasets (Table 2), high values ($r_c, r_{V200} \approx 0.8 - 0.94$) are observed in 4 out of the 6 comparison diagrams (Figures 1 and 2), implying a good compliance of our results with the literature. In contrast, two of these cases show low correlation values ($r_c, r_{V200} \approx 0.3$), specifically in the c_{NFW} comparison diagram (Figure 1, top) and the V_{200}^{BURK} diagram (Figure 2, bottom). These low values are consequence of a handful of outlying galaxies with exceptionally high δ_c or $\delta_{V_{200}}$: one in the c_{NFW} diagram (F571-8) and three in the V_{200}^{BURK} diagram (NGC0247, UGC11557 and D631-7). The main cause for the observed inconsistencies in these galaxies may be attributed to multiple factors, e.g. a divergence from a pure exponential profile in the stellar disk produced by secondary

TABLE 2

COMPARISON WITH LITERATURE VALUES[d]

Profile	$\overline{c}$	$\overline{c_{bib}}$	r_c	t_c	$\overline{V_{200}}$	$\overline{V_{200}^{bib}}$	r_{V200}	t_{V200}
NFW	8.02	9.75	0.3	-0.97	104.16	130.67	0.83	-3.72
ISO	84.39	85.26	0.87	-0.22	99.00	99.22	0.94	0.20
BURK	23.19	23.56	0.78	-0.53	67.45	64.32	0.31	0.49

[d]Results of the t-test analysis between obtained and published (Li et al. 2020) best-fit parameter samples. The first column describes the halo profile, while the second and third columns correspond to the obtained ($\overline{c}$) and the published ($\overline{c_{bib}}$) c parameter sample-average values. Columns 4 and 5 indicate the corresponding Pearson correlation coefficient (r_c) and t-value (t_c) between the c parameter samples. Finally, Columns 6 to 9 describe the obtained ($\overline{V_{200}}$) and published ($\overline{V_{200}^{bib}}$) sample-average values for the parameter V_{200}, along with the corresponding Pearson correlation coefficient (r_{V200}) and t-value (t_{V200}) between the V_{200} parameter samples.

TABLE 3

DEVIATION PARAMETER DISTRIBUTION[e]

	c			V_{200}			c and V_{200}		
$\lvert\delta_i\rvert$	**NFW**	**ISO**	**BURK**	**NFW**	**ISO**	**BURK**	**NFW**	**ISO**	**BURK**
≤ 0.25	66	73	77	76	96	93	63	73	75
≤ 0.5	77	87	87	90	99	96	65	87	86
≤ 0.75	81	94	96	96	99	96	79	94	94
≤ 1	88	96	97	97	99	97	85	95	94

[e]Number of galaxies in our sample with deviation parameter values ($|\delta_c|$ and $|\delta_{V200}|$) below different thresholds.

features (i.e. a bar or bulge), or artifacts produced by the use of different numerical solver routines between studies. Without taking into account the outlying galaxies, the correlation values between the samples are $r_c = 0.93$ and $r_{V200} = 0.92$ for the c_{NFW} and V_{200}^{BURK} comparison diagrams, respectively. It is important to emphasize that these galaxies represent a small fraction of the total sample. Most of the galaxies analysed with our procedure ($\gtrsim 85\%$), show consistency with the literature. The influence of other factors, such as the assumed stellar disc (M/L)* value and the consideration of a separate HI disc component in the resulting mass profile fits, will be explored in a future work.

5.2. *Comparison Between Our Results*

A comparison of our best-fit parameter samples assuming different DM models serves as an internal consistency check for our procedure. Figures 3 and 4 show all the comparison diagrams (ISO vs NFW, BURK vs NFW and BURK vs ISO) between our best-fit parameter samples c and V_{200}, respectively. A qualitative analysis shows that all comparison diagrams display a positive trend, with varying degrees of dispersion. In the case of the c parameter (Figure 3), we found high correlation values ($r \approx 0.9$) in all comparisons, displaying a nearly linear trend. For the case of V_{200}, the diagrams show lower correlation values ($0.43 \leq r \leq 0.71$) and in general, a greater dispersion. This could imply a difference in the sensibility between fitting parameters. From this comparison, we conclude that in general our results show consistency between different models.

6. CONCLUSIONS

The main conclusions of this investigation can be summarized as follows:

1. By using an independent fitting procedure, with its own stellar disc model, optimization algorithm and set of constraints, we were able to marginally replicate the results published in the literature (Li et al. 2020). Our results suggest that the use of a homogenized kinematical data catalogue along with a set of simple physically-based constraints is enough to achieve consistent results, at least with the simplifying assumptions made in the present work.

2. The t-test analysis shows that most of the results obtained here are consistent with those published in the literature, within uncertainties. However, some deviations were observed in a small set of particular galaxies. These inconsistencies could be attributed to multiple causes, like deviations of the stellar disc from an exponential profile (i.e. a bar or bulge), or inconsistencies produced by the use of different numerical solver routines.

3. Our analysis indicates that the use of a different stellar disc model from the one assumed in the literature (Casertano 1983) apparently does not generate large

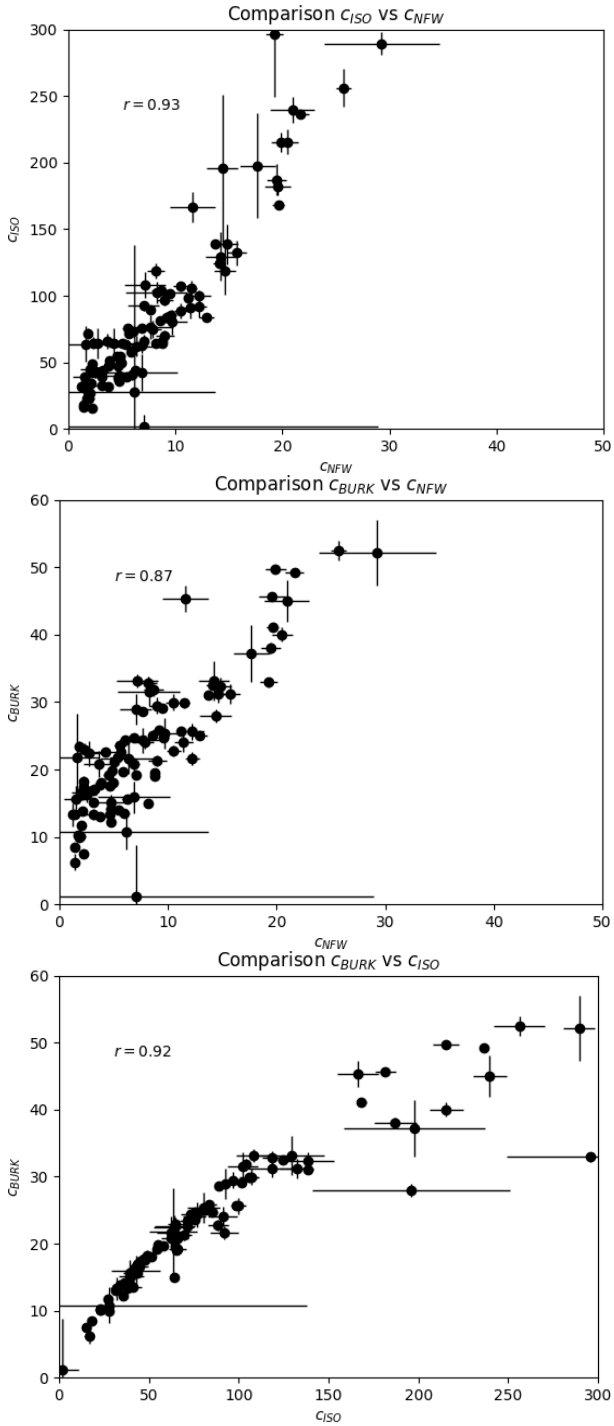

Fig. 3. *Comparison diagrams between our obtained best-fit c samples assuming different DM profiles.*

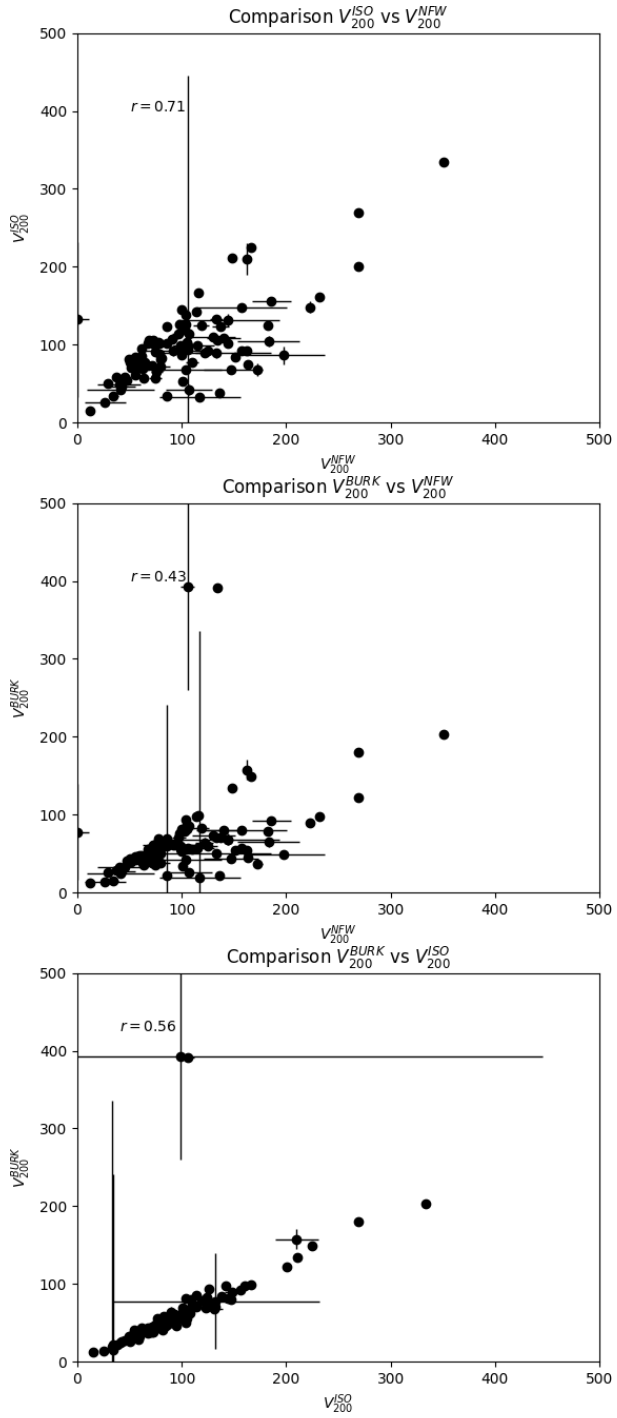

Fig. 4. *Comparison diagrams between our obtained best-fit V_{200} samples assuming different DM profiles.*

deviations in the resulting fits, at least in those cases where a *core* type DM profile (ISO and BURK) is considered. In addition, our assumption of a fixed (M/L)* ratio did not seem to produce any major deviations when compared to the published fits, even when the latter considered a variable (M/L)* ratio, imposing priors around the fiducial (M/L)*=0.5 for the stellar disc (Li et al. 2020).

4. The V_{200}^{NFW} comparison diagram (Figure 2, top), clearly shows a dispersion that is consistently higher

(i.e. not produced by a handful of outlying galaxies) in comparison to the same diagrams for the ISO and BURK profiles. This effect could be explained by two different scenarios: the presence of a bias inherent to the fitting procedure produced by one of its features (e.g. the assumed stellar disk model, optimization algorithm and/or set of constraints), or the fact that a cusp type DM density profile like NFW is simply not adequate to model the RCs of the late-type galaxies analyzed in our test sample, thus producing the observed scatter between studies. This latter scenario is supported by a great amount of evidence obtained over the years, showing a preference for core-type profiles over cusp profiles in late galaxies (McGaugh et al. 2001; Marchesini et al. 2002; Simon et al. 2005; Kuzio de Naray et al. 2008; Walker & Penarrubia 2011). Another reason to support the latter scenario relies on the fact that if our fitting procedure had any inherent bias produced by some its features, we would notice systematic deviations in the results for all the assumed DM profiles, not just for one.

5. As an internal consistency check for our results, a comparison was made between our best fit parameter samples obtained by assuming different DM density models. The qualitative analysis shows that all comparison diagrams (Figures 3 and 4) display a positive trend, with varying degrees of dispersion. The c comparison diagrams display high correlation values between DM models ($r \approx 0.9$), while the corresponding V_{200} diagrams show quite lower values ($0.43 \leq r \leq 0.71$). The difference in the dispersion between the c and V_{200} diagrams is probably caused by a variation in the sensibility between fitting parameters. However, based in the results of this analysis, we conclude that in general our parameter samples are consistent with each other.

6. The analysis of the χ^2_R values in our sample suggests that the best fits are obtained when an ISO DM profile is assumed (i.e. with the lowest sample-averaged χ^2_R), followed by the BURK and finally the NFW profile. From these last results, we conclude that our sample shows a clear tendency to obtain better fits when a core-type profile is assumed. This agrees with a previously published analysis of the sample (Li et al. 2020), providing observational evidence for the *core-cusp* discrepancy.

7. In recent years, homogenized RC+photometry data catalogues such as SPARC (Lelli et al. 2016b), have provided the means to estimate the influence of different optimization algorithms and observational techniques in the search of a consistent RC-fitting procedure that can provide accurate results. This work serves as a first step for a more general approach with our procedure (e.g. adding a bulge component) that would provide a simple, low time-cost method to fit kinematical data for the mass profile estimation of disc galaxies. These latter characteristics would make it suitable for analyzing samples with a great number of galaxies, using photometry data from widely available standardized digital surveys [e.g. SDSS (Abdurro'uf et al. 2022)].

This research was supported by the Instituto Politécnico Nacional (Mexico) under the research projects SIP-20210556, and SIP-20220744. This work is part of MSc. Rodolfo de J. Zermeño's Ph.D. thesis, sponsored by CONACyT. The authors would like to thank Dr. Isaura Fuentes-Carrera, Dr. Janos Zsargó and Dr. Ary Rodríguez for all their valuable discussions and feedback in the preparation of this work. And of course, we sincerely thank the referee for the valuable comments and suggestions in the preparation of this work.

This work is dedicated to the memory of Dr. Héctor Castañeda-Fernández: a beloved researcher, teacher and friend.

APPENDIX

BEST FIT PARAMETER TABLES

Table A1 contains the obtained best-fit values (in tabulated form) of the DM halo parameters for each galaxy in our sample. The complete set of RC plots detailing the velocity contributions for each component (stellar disc, HI disc and DM halo) and tables containing their corresponding best-fit parameter values in machine-readable format, along files with the Asexual Genetic Algorithm (AGA) code in FORTRAN90 language is available to download at the Harvard Dataverse website:
https://dataverse.harvard.edu/privateurl.xhtml?token=66a59351-4b9b-4a1b-a2b5-d25fc4cd5f27
The published data used for comparison in the present work are available to download in machine readable table format at the SPARC catalog website:
http://astroweb.cwru.edu/SPARC/

TABLE A1

BEST-FIT PARAMETER VALUES, ASSUMING A NFW PROFILE.[b]

Name	c	M_{200} ($10^{10} M_{\odot}$)	R_{200} (kpc)	V_{200} (km/s)	$\log \rho_0$ $\left(\frac{M_{\odot}}{pc^3}\right)$	$\log h$ (pc)	χ^2_R
D512-2	6.32 ± 2.54	2.2 ± 22.5	56.3 ± 44.3	41 ± 32	-2.66	3.95	0.41
D564-8	1.17 ± 0.03	19.8 ± 1.5	116.9 ± 2.8	85 ± 2	-4.17	5.00	1.18
D631-7	1.84 ± 0.01	77.5 ± 1.9	184.3 ± 1.5	135 ± 1	-3.81	5.00	8
DDO064	2.36 ± 0.06	163 ± 12	236.4 ± 6.1	173 ± 4	-3.59	5.00	0.73
DDO154	4.93 ± 0.16	8 ± 0.7	86.5 ± 2.4	63 ± 2	-2.91	4.24	12.52
DDO161	1.83 ± 0.14	42.5 ± 6.8	150.8 ± 8.1	110 ± 6	-3.81	4.91	1.42
DDO168	2.23 ± 0.02	136 ± 3.2	222.3 ± 1.8	162 ± 1	-3.65	5.00	11.53
DDO170	5.49 ± 0.28	5.35 ± 0.3	75.6 ± 1.7	55 ± 1	-2.80	4.14	2.02
ESO079-G014	3.69 ± 0.02	623 ± 7.9	369.1 ± 1.6	269 ± 1	-3.18	5.00	4.31
ESO116-G012	6.06 ± 0.48	81.7 ± 12.8	187.6 ± 10.9	137 ± 8	-2.70	4.49	2.99
ESO444-G084	8.18 ± 0.83	16.1 ± 6.3	109.1 ± 12.7	80 ± 9	-2.39	4.13	0.79
ESO563-G021	4.81 ± 0.02	1375 ± 18	480.6 ± 2.1	351 ± 2	-2.93	5.00	23.21
F563-1	7.84 ± 0.86	29 ± 6	132.8 ± 9.1	97 ± 7	-2.43	4.23	1.04
F563-V1	6.11 ± 7.64	0.06 ± 0.1	17.1 ± 5.7	12 ± 4	-2.69	3.45	0.36
F563-V2	7.17 ± 1.89	95.7 ± 177	198 ± 67	144 ± 49	-2.53	4.44	1.3
F565-V2	2.5 ± 0.88	196 ± 64	251 ± 40	183 ± 29	-3.54	5.00	0.4
F567-2	6.8 ± 3.3	2 ± 11.4	55 ± 29	40 ± 21	-2.58	3.90	0.47
F568-1	7.01 ± 1.46	124 ± 188	215.4 ± 59.4	157 ± 43	-2.55	4.49	0.82
F568-3	2.5 ± 0.03	194 ± 6.8	250.3 ± 3	183 ± 2	-3.54	5.00	3.35
F568-V1	14.62 ± 0.99	20.1 ± 2.5	117.6 ± 4.8	86 ± 3	-1.77	3.91	0.21
F571-8	5.56 ± 0.57	204 ± 69	254.4 ± 25.4	186 ± 19	-2.78	4.66	1.07
F571-V1	4.69 ± 1.56	24.6 ± 39.8	125.7 ± 40	92 ± 29	-2.95	4.43	0.34
F574-1	8.61 ± 0.34	20 ± 1.6	117.5 ± 3.2	86 ± 2	-2.34	4.14	1.46
F574-2	7.05 ± 21.87	0 ± 0.5	0 ± 15.8	0 ± 12	-2.54	-0.33	0.17
F579-V1	20.93 ± 2.09	9.7 ± 0.9	92.2 ± 3	67 ± 2	-1.37	3.64	0.21
F583-1	4.61 ± 0.28	30.4 ± 5.7	134.9 ± 8.2	98 ± 6	-2.97	4.47	1.63
F583-4	3.63 ± 1.39	36 ± 50	142.8 ± 47.1	104 ± 34	-3.20	4.59	0.17
IC2574	1.44 ± 0	37.2 ± 0.3	144.2 ± 0.4	105 ± 0	-4.01	5.00	43.75
KK98-251	1.39 ± 0.03	33.1 ± 2.2	138.8 ± 3.1	101 ± 2	-4.04	5.00	2.08
NGC0024	21.63 ± 0.87	10.1 ± 0.7	93.4 ± 2.1	68 ± 2	-1.34	3.64	0.95
NGC0055	3.12 ± 0.27	61.6 ± 13.7	170.7 ± 12.6	125 ± 9	-3.34	4.74	1.4
NGC0247	5.64 ± 0.24	31.9 ± 3.8	137.1 ± 5.3	100 ± 4	-2.77	4.39	1.75
NGC1003	4.72 ± 0.1	38.8 ± 1.2	146.3 ± 1.5	107 ± 1	-2.95	4.49	2.78
NGC2403	11.24 ± 0.07	29.7 ± 0.3	133.9 ± 0.4	98 ± 0	-2.05	4.08	11.41
NGC3109	2.15 ± 0.01	123.7 ± 2.2	215.3 ± 1.3	157 ± 1	-3.67	5.00	10.17
NGC3198	8.77 ± 0.07	47.2 ± 0.5	156.2 ± 0.6	114 ± 0	-2.32	4.25	2.57
NGC3741	3.83 ± 0.41	13.3 ± 3.4	102.4 ± 8.8	75 ± 6	-3.15	4.43	0.37
NGC3769	14.38 ± 1.48	14.9 ± 1.7	106.3 ± 4.1	78 ± 3	-1.79	3.87	0.69
NGC3893	17.69 ± 1.62	32.1 ± 4.6	137.3 ± 6.5	100 ± 5	-1.56	3.89	0.55
NGC3917	3.18 ± 0.02	397.9 ± 6.3	317.9 ± 1.7	232 ± 1	-3.32	5.00	7.5
NGC3992	12.23 ± 0.68	145.8 ± 6.2	227.5 ± 3.3	166 ± 2	-1.96	4.27	1.27
NGC4010	3.05 ± 0.03	350.4 ± 11.6	304.7 ± 3.3	222 ± 2	-3.36	5.00	2.49
NGC4100	12.92 ± 0.7	50.2 ± 4	159.4 ± 4.1	116 ± 3	-1.90	4.09	3.58
NGC4183	10.52 ± 0.64	15.5 ± 1.2	107.7 ± 2.7	79 ± 2	-2.12	4.01	0.18
NGC4559	4.71 ± 0.44	53.1 ± 11.2	162.5 ± 10.6	119 ± 8	-2.95	4.54	0.81
NGC5585	5.06 ± 0.12	37.7 ± 2.2	144.9 ± 3	106 ± 2	-2.88	4.46	8.93
NGC6015	13.74 ± 0.2	35.3 ± 0.8	141.7 ± 1.1	103 ± 1	-1.84	4.01	6.55
NGC7793	10.48 ± 0.72	13.4 ± 2.1	102.6 ± 5.1	75 ± 4	-2.13	3.99	1.19
UGC00128	8.21 ± 0.08	35.3 ± 0.3	141.8 ± 0.4	104 ± 0	-2.39	4.24	2.97
UGC00191	9.52 ± 0.24	8.4 ± 0.3	87.9 ± 0.9	64 ± 1	-2.23	3.97	3.12
UGC00634	6.25 ± 0.53	34.8 ± 5.8	141.1 ± 7.4	103 ± 5	-2.67	4.35	3.3
UGC00731	9.57 ± 0.51	5.9 ± 0.6	78 ± 2.4	57 ± 2	-2.23	3.91	0.33
UGC00891	2.08 ± 0.01	110.6 ± 1.3	207.4 ± 0.8	151 ± 1	-3.71	5.00	3.49
UGC01230	11.44 ± 0.85	14.9 ± 1.9	106.4 ± 4.2	78 ± 3	-2.04	3.97	1.01
UGC02259	19.48 ± 0.89	5.5 ± 0.3	76.2 ± 1.2	56 ± 1	-1.45	3.59	0.69
UGC04325	19.56 ± 1.2	7.4 ± 0.8	84.4 ± 3.1	62 ± 2	-1.45	3.63	3.11
UGC04483	8.25 ± 2.88	0.6 ± 4.7	36.3 ± 26.7	26 ± 19	-2.38	3.64	0.71
UGC04499	6.81 ± 0.59	10 ± 2.2	93.1 ± 6.3	68 ± 5	-2.58	4.14	0.62
UGC05005	1.91 ± 0.52	86.9 ± 23.3	191.4 ± 22	140 ± 16	-3.78	5.00	0.24
UGC05414	2.24 ± 0.03	138.7 ± 6.4	223.7 ± 3.4	163 ± 2	-3.64	5.00	1.26
UGC05716	8.74 ± 0.11	6.7 ± 0.1	81.5 ± 0.6	59 ± 0	-2.32	3.97	2.01
UGC05721	25.7 ± 0.72	3.7 ± 0.1	67 ± 0.9	49 ± 1	-1.14	3.42	1.08

TABLE A1. CONTINUED

Name	c	M_{200} ($10^{10} M_\odot$)	R_{200} (kpc)	V_{200} (km/s)	$\log \rho_0$ $\left(\frac{M_\odot}{pc^3}\right)$	$\log h$ (pc)	χ^2_R
UGC05750	1.67 ± 0.18	57.4 ± 10.7	166.7 ± 11.6	122 ± 8	-3.89	5.00	1.16
UGC05764	19.62 ± 0.52	1.7 ± 0.1	51.4 ± 0.8	38 ± 1	-1.45	3.42	6.61
UGC05829	2.01 ± 0.89	101 ± 34	201.3 ± 35.8	147 ± 26	-3.73	5.00	0.1
UGC05918	7.67 ± 2.09	2.4 ± 4.9	57.5 ± 18.9	42 ± 14	-2.46	3.88	0.15
UGC05986	7.67 ± 0.38	75.6 ± 10.9	182.7 ± 8.4	133 ± 6	-2.46	4.38	7.69
UGC05999	3.13 ± 0.82	70 ± 33	178 ± 28	130 ± 21	-3.34	4.76	2.23
UGC06399	5.4 ± 0.7	48 ± 28	157 ± 23	115 ± 17	-2.82	4.47	0.74
UGC06446	14.8 ± 1	6 ± 0.6	78.4 ± 2.6	57 ± 2	-1.75	3.72	0.22
UGC06667	6.86 ± 0.66	31 ± 7	135.9 ± 10.3	99 ± 8	-2.57	4.30	1.29
UGC06917	9.16 ± 0.62	23.7 ± 4	124.1 ± 6.6	91 ± 5	-2.27	4.13	0.38
UGC06923	4.28 ± 1.73	75.3 ± 113	182.5 ± 71.8	133 ± 52	-3.04	4.63	0.61
UGC06930	12.25 ± 1.11	12.8 ± 1.5	101.2 ± 4.1	74 ± 3	-1.96	3.92	0.17
UGC06983	15.72 ± 0.92	12.4 ± 0.7	99.9 ± 2	73 ± 1	-1.69	3.80	0.53
UGC07089	1.97 ± 0.04	95.1 ± 6.5	197.3 ± 4.4	144 ± 3	-3.75	5.00	0.74
UGC07125	5.96 ± 0.49	3.4 ± 0.3	64.9 ± 1.8	47 ± 1	-2.72	4.04	0.55
UGC07151	9.02 ± 0.76	7.9 ± 1.8	85.9 ± 6.3	63 ± 5	-2.29	3.98	2.83
UGC07261	14.25 ± 1.41	4.3 ± 0.9	70.2 ± 4.6	51 ± 3	-1.80	3.69	0.04
UGC07399	19.9 ± 0.95	11 ± 1	96.1 ± 3	70 ± 2	-1.43	3.68	0.74
UGC07524	5.87 ± 0.43	15.8 ± 2.3	108.5 ± 5.4	79 ± 4	-2.73	4.27	0.56
UGC07559	1.47 ± 1.02	38.7 ± 13.3	146.2 ± 30.8	107 ± 22	-4.00	5.00	0.64
UGC07603	8.7 ± 0.9	11.6 ± 5.8	97.9 ± 12.3	71 ± 9	-2.33	4.05	1.9
UGC07608	2.71 ± 1.1	247 ± 82	271 ± 53	198 ± 39	-3.47	5.00	0.45
UGC07690	29.3 ± 5.4	0.8 ± 0.2	40 ± 2.7	29 ± 2	-0.99	3.14	0.18
UGC07866	1.63 ± 2.05	51 ± 25	160.3 ± 53.1	117 ± 39	-3.91	4.99	0.05
UGC08286	14 ± 0.53	7.4 ± 0.4	84.2 ± 1.6	61 ± 1	-1.81	3.78	2.68
UGC08490	20.48 ± 0.97	4.2 ± 0.2	69.7 ± 1.2	51 ± 1	-1.40	3.53	0.11
UGC08550	11.5 ± 0.48	3.06 ± 0.3	62.8 ± 2	46 ± 1	-2.03	3.74	1.74
UGC09037	2.23 ± 0.03	136.7 ± 4.8	222.7 ± 2.5	163 ± 2	-3.65	5.00	3.32
UGC10310	9.72 ± 1.4	5.8 ± 1.5	77.6 ± 6.6	57 ± 5	-2.21	3.90	0.68
UGC11455	3.69 ± 0.03	623 ± 15	369.2 ± 2.9	269 ± 2	-3.18	5.00	5.86
UGC11557	1.45 ± 0.09	37.4 ± 7.6	144.6 ± 9.3	106 ± 7	-4.01	5.00	1.44
UGC11820	4.68 ± 0.32	16.6 ± 1.9	110.3 ± 4.2	81 ± 3	-2.96	4.37	2.02
UGC12506	19.25 ± 0.84	102.8 ± 4.1	202.4 ± 2.7	148 ± 2	-1.47	4.02	0.15
UGC12632	9.01 ± 0.87	5.9 ± 1	77.9 ± 4.1	57 ± 3	-2.29	3.94	0.31
UGC12732	7.03 ± 0.34	15.6 ± 1.4	107.9 ± 3.2	79 ± 2	-2.55	4.19	0.19
UGCA281	11.6 ± 2.11	1.3 ± 0.5	47.2 ± 6.4	34 ± 5	-2.02	3.61	1.03
UGCA442	4.53 ± 0.46	14 ± 3	104 ± 7.7	76 ± 6	-2.99	4.36	2.18
UGCA444	1.86 ± 0.02	79.5 ± 3	185.8 ± 2.3	136 ± 2	-3.80	5.00	0.06

[b]Best-fit parameter values, assuming a NFW profile. Column 1 the galaxy name as listed in Table 1, while c, M_{200}, R_{200} and V_{200} are listed in Columns 2, 3, 4 and 5, respectively. In Columns 6 and 7 are shown the core density (ρ_0) and the scale length (h) of the DM halo, respectively. Finally, the χ^2_R values are given in Column 8.

TABLE A2

BEST-FIT PARAMETER VALUES, ASSUMING AN ISO PROFILE.[c]

Name	c	M_{200} ($10^{10} M_\odot$)	R_{200} (kpc)	V_{200} (km/s)	$\log \rho_0$ $\left(\frac{M_\odot}{pc^3}\right)$	$\log h$ (pc)	χ^2_R
D512-2	62.24 ± 7.7	2.33 ± 0.3	57.3 ± 2.8	42 ± 2	-1.41	2.96	0.16
D564-8	32.07 ± 3.76	1.26 ± 0.4	46.7 ± 4.8	34 ± 3	-1.97	3.16	0.11
D631-7	27.59 ± 0.62	37.68 ± 5.7	144.9 ± 7.7	106 ± 6	-2.10	3.72	1.8
DDO064	64.5 ± 4.3	9.74 ± 3.9	92.3 ± 11.1	67 ± 8	-1.38	3.16	0.31
DDO154	49.53 ± 0.3	6.08 ± 0.1	78.9 ± 0.4	58 ± 0	-1.60	3.20	2.65
DDO161	23.09 ± 0.32	14.4 ± 0.3	105.1 ± 0.6	77 ± 0	-2.25	3.66	0.29
DDO168	45.16 ± 0.82	25.36 ± 2.3	127 ± 3.7	93 ± 3	-1.68	3.45	4.36
DDO170	39.27 ± 1.34	7.51 ± 0.3	84.6 ± 1	62 ± 1	-1.80	3.33	1.2
ESO079-G014	46.89 ± 1.13	257.64 ± 11.5	275 ± 4.1	201 ± 3	-1.65	3.77	1.47
ESO116-G012	73.17 ± 2.68	60.39 ± 2.1	169.6 ± 2	124 ± 1	-1.27	3.36	1.1
ESO444-G084	118.62 ± 5.41	11.57 ± 0.7	97.7 ± 2	71 ± 1	-0.85	2.92	0.93
ESO563-G021	54.79 ± 0.86	1184.47 ± 29	457.3 ± 3.7	334 ± 3	-1.52	3.92	13.38
F563-1	75.18 ± 6.47	47.05 ± 4.3	156 ± 4.9	114 ± 4	-1.24	3.32	0.54
F563-V1	27.55 ± 110.35	0.11 ± 0.1	20.7 ± 3.7	15 ± 3	-2.10	2.88	0.36
F563-V2	108.31 ± 9.61	71.89 ± 12.5	179.7 ± 10.6	131 ± 8	-0.93	3.22	0.33
F565-V2	42.02 ± 4.03	36.24 ± 7.3	143 ± 9.6	104 ± 7	-1.74	3.53	0.06
F567-2	42.66 ± 13.74	3.75 ± 0.8	67.2 ± 4.9	49 ± 4	-1.73	3.20	0.36
F568-1	92.36 ± 3.75	101.29 ± 7	201.5 ± 4.4	147 ± 3	-1.07	3.34	0.12
F568-3	42.89 ± 0.97	62.28 ± 4.6	171.3 ± 4.3	125 ± 3	-1.73	3.60	1.03
F568-V1	118.58 ± 17.92	59.01 ± 7.4	168.3 ± 7	123 ± 5	-0.85	3.15	0.13
F571-8	75.35 ± 1.28	120.54 ± 4.3	213.5 ± 2.5	156 ± 2	-1.24	3.45	1.34
F571-V1	40.18 ± 6.85	25.32 ± 5.8	126.9 ± 8.9	93 ± 6	-1.78	3.50	0.08
F574-1	81.15 ± 2.16	33.09 ± 1.1	138.7 ± 1.5	101 ± 1	-1.18	3.23	0.19
F574-2	1.82 ± 0.2	73.96 ± 50	181.4 ± 17	132 ± 13	-4.10	5.00	0.13
F579-V1	239.65 ± 9.5	33.51 ± 2.2	139.3 ± 3	102 ± 2	-0.24	2.76	0.06
F583-1	47.61 ± 0.88	27.06 ± 1.4	129.7 ± 2.4	95 ± 2	-1.64	3.44	0.36
F583-4	65.82 ± 5.95	9.93 ± 0.8	92.9 ± 2.5	68 ± 2	-1.36	3.15	0.31
IC2574	18.3 ± 0.23	35.56 ± 3.8	142.1 ± 4.9	104 ± 4	-2.44	3.89	1.98
KK98-251	32.32 ± 1.21	4.62 ± 1.1	72 ± 5.5	53 ± 4	-1.97	3.35	0.3
NGC0024	236.4 ± 2.17	37.02 ± 0.8	144 ± 1	105 ± 1	-0.26	2.78	0.35
NGC0055	39.15 ± 0.74	25.24 ± 1.3	126.8 ± 2.2	93 ± 2	-1.80	3.51	0.23
NGC0247	71.24 ± 1.38	21.22 ± 0.7	119.6 ± 1.2	87 ± 1	-1.29	3.23	2.61
NGC1003	35.97 ± 0.92	47.4 ± 0.8	156.4 ± 0.8	114 ± 1	-1.88	3.64	3.21
NGC2403	98.73 ± 0.53	64.25 ± 0.2	173.1 ± 0.2	126 ± 0	-1.01	3.24	16.89
NGC3109	42.31 ± 0.88	25.02 ± 1.7	126.4 ± 2.9	92 ± 2	-1.74	3.48	0.16
NGC3198	65.53 ± 0.92	91.01 ± 0.5	194.4 ± 0.4	142 ± 0	-1.36	3.47	1.67
NGC3741	51.29 ± 1.51	5.77 ± 0.4	77.5 ± 1.7	57 ± 1	-1.57	3.18	0.91
NGC3769	195.74 ± 55.12	35.03 ± 2.2	141.4 ± 2.8	103 ± 2	-0.42	2.86	0.28
NGC3893	197.8 ± 39.28	95.98 ± 5.1	197.9 ± 3.5	144 ± 3	-0.41	3.00	0.54
NGC3917	43.99 ± 1.08	131.99 ± 3.2	220 ± 1.8	161 ± 1	-1.70	3.70	3.36
NGC3992	91.91 ± 8.04	360.5 ± 7	307.6 ± 1.9	225 ± 1	-1.07	3.52	1.57
NGC4010	43.28 ± 2.32	104 ± 16.3	203.3 ± 10.4	148 ± 8	-1.72	3.67	1.31
NGC4100	83.77 ± 2.68	147.33 ± 3	228.3 ± 1.6	167 ± 1	-1.15	3.44	3.22
NGC4183	88.46 ± 5.6	33.16 ± 0.8	138.8 ± 1.1	101 ± 1	-1.11	3.20	0.21
NGC4559	36.42 ± 1.58	61.21 ± 3.9	170.3 ± 3.7	124 ± 3	-1.86	3.67	0.41
NGC5585	64.06 ± 1.55	26.27 ± 0.6	128.5 ± 1	94 ± 1	-1.38	3.30	20.67
NGC6015	138.63 ± 2.82	83.73 ± 1.3	189.1 ± 0.9	138 ± 1	-0.72	3.13	5.76
NGC7793	107 ± 3.54	23.87 ± 2.1	124.4 ± 3.6	91 ± 3	-0.94	3.07	1.52
UGC00128	64.19 ± 0.59	63.92 ± 0.2	172.8 ± 0.1	126 ± 0	-1.38	3.43	3.33
UGC00191	101.7 ± 2.25	14.8 ± 0.2	106.1 ± 0.5	77 ± 0	-0.98	3.02	1.16
UGC00634	43.69 ± 2.41	53.78 ± 2.5	163.1 ± 2.5	119 ± 2	-1.71	3.57	1.55
UGC00731	85.58 ± 2.57	11.22 ± 0.6	96.7 ± 1.6	71 ± 1	-1.13	3.05	0.17
UGC00891	33.9 ± 0.93	19.09 ± 1.1	115.5 ± 2.4	84 ± 2	-1.93	3.53	0.2
UGC01230	91.05 ± 8.14	33.03 ± 2.7	138.7 ± 3.5	101 ± 3	-1.08	3.18	0.74
UGC02259	187 ± 11.9	19.33 ± 0.5	116 ± 1	85 ± 1	-0.46	2.79	0.48
UGC04325	181.7 ± 5.9	27.35 ± 1	130.2 ± 1.5	95 ± 1	-0.48	2.86	1.53
UGC04483	102.4 ± 8	0.53 ± 0.1	35 ± 1.2	26 ± 1	-0.98	2.53	0.31
UGC04499	62.6 ± 5.6	12.81 ± 1.4	101.1 ± 3.5	74 ± 3	-1.40	3.21	0.12
UGC05005	23.2 ± 1.9	40.66 ± 6.1	148.6 ± 7.3	108 ± 5	-2.25	3.81	0.03
UGC05414	48.9 ± 2.8	13.37 ± 1.6	102.6 ± 4.4	75 ± 3	-1.61	3.32	0.08
UGC05716	64.48 ± 1.25	13.03 ± 0.2	101.7 ± 0.6	74 ± 0	-1.38	3.20	2.57
UGC05721	256.2 ± 14	17 ± 0.8	111 ± 1.8	81 ± 1	-0.19	2.64	0.88

TABLE A2. CONTINUED

Name	c	M_{200} ($10^{10} M_\odot$)	R_{200} (kpc)	V_{200} (km/s)	$\log \rho_0$ $\left(\frac{M_\odot}{pc^3}\right)$	$\log h$ (pc)	χ^2_R
UGC05750	23.12 ± 1.41	22.72 ± 3.4	122.4 ± 6.5	89 ± 5	-2.25	3.72	0.3
UGC05764	168.37 ± 2.91	6.38 ± 0.1	80.1 ± 0.3	59 ± 0	-0.55	2.68	4.37
UGC05829	45 ± 4.41	9.82 ± 3	92.6 ± 7.8	68 ± 6	-1.68	3.31	0.14
UGC05918	76.69 ± 8.84	3.06 ± 0.4	62.8 ± 2.9	46 ± 2	-1.23	2.91	0.01
UGC05986	89.13 ± 2.07	74.01 ± 1.9	181.4 ± 1.5	132 ± 1	-1.10	3.31	2.54
UGC05999	32.56 ± 1.68	42.51 ± 4.4	150.8 ± 5.5	110 ± 4	-1.96	3.67	0.96
UGC06399	63.32 ± 2.84	31.27 ± 5.7	136.2 ± 7.7	99 ± 6	-1.39	3.33	0.11
UGC06446	138.58 ± 14.65	16.34 ± 1.1	109.7 ± 2.5	80 ± 2	-0.72	2.90	0.2
UGC06667	75.4 ± 3.18	30.35 ± 1.4	134.8 ± 2.1	98 ± 2	-1.24	3.25	0.21
UGC06917	83.7 ± 3.89	39.8 ± 2.8	147.6 ± 3.4	108 ± 2	-1.15	3.25	0.17
UGC06923	64.64 ± 11.26	22.7 ± 4.5	122.4 ± 8.2	89 ± 6	-1.37	3.28	0.41
UGC06930	99.63 ± 4.11	31.6 ± 0.8	136.6 ± 1.1	100 ± 1	-1.00	3.14	0.1
UGC06983	132.3 ± 9.23	37.39 ± 1.5	144.5 ± 1.9	105 ± 1	-0.76	3.04	0.48
UGC07089	27.23 ± 0.7	33.18 ± 2.5	138.9 ± 3.6	101 ± 3	-2.11	3.71	0.08
UGC07125	41.14 ± 4.85	5.25 ± 0.3	75.1 ± 1.5	55 ± 1	-1.76	3.26	0.35
UGC07151	96.94 ± 4.58	10.63 ± 0.5	95 ± 1.6	69 ± 1	-1.03	2.99	1.27
UGC07261	129.54 ± 18.26	11.48 ± 1.3	97.5 ± 3.6	71 ± 3	-0.78	2.88	0.02
UGC07399	215.14 ± 7.26	36.14 ± 0.7	142.9 ± 0.9	104 ± 1	-0.34	2.82	0.24
UGC07524	58.18 ± 1.97	16.86 ± 0.6	110.8 ± 1.3	81 ± 1	-1.46	3.28	0.43
UGC07559	39.21 ± 3.41	2.4 ± 1.3	57.8 ± 8.9	42 ± 6	-1.80	3.17	0.16
UGC07603	103.94 ± 2.73	12.31 ± 0.5	99.8 ± 1.4	73 ± 1	-0.97	2.98	0.5
UGC07608	64.07 ± 11.2	20.45 ± 9.8	118.2 ± 15.3	86 ± 11	-1.38	3.27	0.06
UGC07690	289.45 ± 8.66	3.97 ± 0.3	68.5 ± 1.7	50 ± 1	-0.08	2.37	0.25
UGC07866	63.6 ± 13.43	1.13 ± 0.4	45 ± 4.8	33 ± 3	-1.39	2.85	0.04
UGC08286	124.71 ± 3.38	19.91 ± 0.1	117.1 ± 0.2	86 ± 0	-0.81	2.97	0.81
UGC08490	215.43 ± 9.38	14.68 ± 0.2	105.8 ± 0.5	77 ± 0	-0.34	2.69	0.2
UGC08550	105.71 ± 5.43	6.57 ± 0.2	80.9 ± 0.9	59 ± 1	-0.95	2.88	0.67
UGC09037	15.41 ± 0.38	295.1 ± 106	287.7 ± 28	210 ± 21	-2.59	4.27	1
UGC10310	80.27 ± 9.14	11.71 ± 1.4	98.1 ± 4	72 ± 3	-1.19	3.09	0.31
UGC11455	31.59 ± 0.65	618.55 ± 15.5	368.2 ± 3.1	269 ± 2	-1.99	4.07	2.54
UGC11557	16.72 ± 2.76	30 ± 11	135 ± 18	99 ± 13	-2.52	3.91	0.94
UGC11820	38.23 ± 0.85	18.19 ± 0.3	113.7 ± 0.6	83 ± 0	-1.82	3.47	8.64
UGC12506	296.1 ± 47	299 ± 10.6	289 ± 3.4	211 ± 2	-0.06	2.99	0.27
UGC12632	69.73 ± 3.96	11.5 ± 0.4	97.6 ± 1.2	71 ± 1	-1.31	3.15	0.12
UGC12732	65.88 ± 4.79	22.03 ± 1.2	121.2 ± 2.2	88 ± 2	-1.36	3.26	0.48
UGCA281	166.34 ± 11.23	1.3 ± 0.2	47.1 ± 2	34 ± 1	-0.56	2.45	0.23
UGCA442	54.17 ± 1.6	8.87 ± 0.3	89.5 ± 1	65 ± 1	-1.53	3.22	0.72
UGCA444	71.29 ± 4.01	1.72 ± 0.2	51.8 ± 1.9	38 ± 1	-1.29	2.86	0.21

[c]Best-fit parameter values, assuming an ISO profile. Columns as in Table A1.

TABLE A3

BEST-FIT PARAMETER VALUES, ASSUMING A BURK PROFILE.[d]

Name	c	M_{200} ($10^{10} M_{\odot}$)	R_{200} (kpc)	V_{200} (km/s)	$\log \rho_0$ $\left(\frac{M_{\odot}}{pc^3}\right)$	$\log h$ (pc)	χ^2_R
D512-2	21.67 ± 2.38	0.46 ± 0.2	33.4 ± 4.5	24 ± 3	-1.37	3.19	0.08
D564-8	13.27 ± 0.6	0.35 ± 0.08	30.4 ± 2	22 ± 1.6	-1.91	3.36	0.12
D631-7	9.9 ± 0.1	1910 ± 39	536 ± 4	391 ± 3	-2.23	4.73	3.72
DDO064	23 ± 1	1.6 ± 0.3	50 ± 3	36 ± 2	-1.30	3.34	0.31
DDO154	18.1 ± 0.07	1.38 ± 0	48.1 ± 0.2	35 ± 0	-1.57	3.42	1.37
DDO161	10.08 ± 0.14	5.35 ± 0.2	75.6 ± 0.8	55 ± 1	-2.21	3.88	0.22
DDO168	17.35 ± 0.34	5.29 ± 1.6	75.3 ± 6.6	55 ± 5	-1.62	3.64	4.54
DDO170	13.96 ± 0.33	2.57 ± 0.1	59.2 ± 0.9	43 ± 1	-1.86	3.63	1.6
ESO079-G014	17.69 ± 0.51	57.91 ± 3.5	167.2 ± 3.4	122 ± 2	-1.59	3.98	1.25
ESO116-G012	24.32 ± 0.51	11 ± 0.6	96.1 ± 1.7	70 ± 1	-1.24	3.60	0.82
ESO444-G084	32.84 ± 1.02	1.74 ± 0.1	52 ± 1.3	38 ± 1	-0.89	3.20	1.33
ESO563-G021	19.9 ± 0.2	266.3 ± 0.9	278 ± 0.3	203 ± 0	-1.46	4.15	13.14
F563-1	24.03 ± 0.99	11.2 ± 1	96.7 ± 2.8	71 ± 2	-1.25	3.60	0.54
F563-V1	10.81 ± 2.68	0.06 ± 0	16.5 ± 2.2	12 ± 2	-2.13	3.18	0.3
F563-V2	33.12 ± 0.97	10.28 ± 1.5	94 ± 4.7	69 ± 3	-0.88	3.45	0.21
F565-V2	16.28 ± 1.15	8.63 ± 2.9	88.6 ± 8.4	65 ± 6	-1.69	3.74	0.06
F567-2	15.88 ± 2.33	1.08 ± 0.3	44.3 ± 4.5	32 ± 3	-1.71	3.45	0.26
F568-1	28.97 ± 2.24	16.34 ± 2.9	109.7 ± 6.5	80 ± 5	-1.04	3.58	0.08
F568-3	16.56 ± 0.39	15.22 ± 2.3	107.1 ± 5.2	78 ± 4	-1.67	3.81	1.03
F568-V1	31.26 ± 1.3	10.37 ± 1.2	94.3 ± 3.5	69 ± 3	-0.95	3.48	0.05
F571-8	23.64 ± 0.61	24.93 ± 2.1	126.3 ± 3.4	92 ± 3	-1.27	3.73	1.64
F571-V1	15.14 ± 1.09	7.31 ± 1.1	83.9 ± 3.8	61 ± 3	-1.77	3.74	0.04
F574-1	25.03 ± 0.47	6.88 ± 0.4	82.2 ± 1.7	60 ± 1	-1.20	3.52	0.05
F574-2	1.1 ± 7.68	14.8 ± 37	106 ± 84	77 ± 62	-4.07	4.98	0.13
F579-V1	44.96 ± 3.06	5.47 ± 0.3	76.2 ± 1.5	56 ± 1	-0.53	3.23	0.36
F583-1	17.56 ± 0.17	6.83 ± 0.2	82 ± 0.9	60 ± 1	-1.60	3.67	0.21
F583-4	20.81 ± 1.98	2.33 ± 1.2	57.3 ± 7	42 ± 5	-1.41	3.44	0.45
IC2574	8.4 ± 0.09	16.81 ± 2	110.7 ± 4.7	81 ± 3	-2.40	4.12	1.76
KK98-251	13.33 ± 0.2	1.26 ± 0.3	46.6 ± 3.5	34 ± 3	-1.91	3.54	0.32
NGC0024	49.19 ± 0.46	5.65 ± 0.1	77 ± 0.6	56 ± 0	-0.43	3.19	0.73
NGC0055	15.05 ± 0.12	6.99 ± 0.3	82.7 ± 1.1	60 ± 1	-1.77	3.74	0.19
NGC0247	22.68 ± 0.31	4.65 ± 0.2	72.1 ± 1	53 ± 1	-1.32	3.50	4.88
NGC1003	12.19 ± 0.17	19.66 ± 0.4	116.6 ± 0.8	85 ± 1	-2.00	3.98	5.12
NGC2403	25.64 ± 0.02	14.01 ± 0	104.2 ± 0.1	76 ± 0	-1.18	3.61	24.35
NGC3109	16.28 ± 0.25	5.94 ± 0.4	78.3 ± 1.8	57 ± 1	-1.69	3.68	0.16
NGC3198	19.05 ± 0.07	30.09 ± 0.2	134.4 ± 0.3	98 ± 0	-1.51	3.85	1.26
NGC3741	18.03 ± 0.28	1.47 ± 0.1	49.2 ± 0.8	36 ± 1	-1.57	3.44	1.05
NGC3769	27.9 ± 0.96	9.44 ± 0.2	91.3 ± 0.8	67 ± 1	-1.08	3.51	1.66
NGC3893	37.24 ± 4.22	17.22 ± 2.1	111.6 ± 4.6	81 ± 3	-0.75	3.48	1.43
NGC3917	17 ± 0.28	29.71 ± 2.4	133.9 ± 3.6	98 ± 3	-1.64	3.90	3.32
NGC3992	21.62 ± 1.01	104.81 ± 5.4	203.8 ± 3.5	149 ± 3	-1.37	3.97	0.64
NGC4010	16.95 ± 0.35	22.43 ± 1.9	121.9 ± 3.7	89 ± 3	-1.64	3.86	1.25
NGC4100	25.04 ± 0.35	31.06 ± 0.7	135.9 ± 1	99 ± 1	-1.20	3.73	2.08
NGC4183	22.79 ± 0.76	8.98 ± 0.3	89.8 ± 1.2	66 ± 1	-1.31	3.60	0.41
NGC4559	14.1 ± 0.48	18.4 ± 1.3	114.1 ± 2.7	83 ± 2	-1.84	3.91	0.26
NGC5585	21.21 ± 0.15	6.13 ± 0.1	79.1 ± 0.4	58 ± 0	-1.39	3.57	20.46
NGC6015	31.03 ± 0.15	18.82 ± 0.1	115 ± 0.2	84 ± 0	-0.96	3.57	12.43
NGC7793	29.95 ± 1.23	4.36 ± 0.3	70.6 ± 1.6	52 ± 1	-1.00	3.37	1.44
UGC00128	14.99 ± 0.13	25.87 ± 0.3	127.8 ± 0.5	93 ± 0	-1.78	3.93	7.83
UGC00191	29.15 ± 0.39	2.98 ± 0.1	62.2 ± 0.4	45 ± 0	-1.03	3.33	4.1
UGC00634	15.56 ± 0.52	15.75 ± 1	108.3 ± 2.3	79 ± 2	-1.74	3.84	0.39
UGC00731	24.76 ± 0.4	2.56 ± 0.1	59.1 ± 0.9	43 ± 1	-1.22	3.38	0.6
UGC00891	13.79 ± 0.37	5.15 ± 0.6	74.6 ± 2.6	54 ± 2	-1.87	3.73	0.17
UGC01230	24.06 ± 1.39	10.46 ± 0.6	94.5 ± 1.7	69 ± 1	-1.25	3.59	0.23
UGC02259	38 ± 0.82	3.14 ± 0.1	63.3 ± 0.4	46 ± 0	-0.73	3.22	2.19
UGC04325	45.64 ± 0.52	3.2 ± 0.1	63.7 ± 0.6	46 ± 0	-0.51	3.14	0.39
UGC04483	31.52 ± 2.09	0.07 ± 0	18.1 ± 0.8	13 ± 1	-0.94	2.76	0.29
UGC04499	20.82 ± 0.99	2.92 ± 0.2	61.8 ± 1.2	45 ± 1	-1.41	3.47	0.15
UGC05005	10.08 ± 0.26	16.36 ± 2.4	109.7 ± 5.4	80 ± 4	-2.21	4.04	0.01
UGC05414	18.28 ± 0.68	2.83 ± 0.8	61.1 ± 5.1	45 ± 4	-1.56	3.52	0.08
UGC05716	19.51 ± 0.18	3.53 ± 0.1	65.8 ± 0.4	48 ± 0	-1.49	3.53	3.75
UGC05721	52.44 ± 1.45	2.1 ± 0.1	55.4 ± 0.8	40 ± 1	-0.35	3.02	0.41

TABLE A3. CONTINUED

Name	c	M_{200} ($10^{10} M_\odot$)	R_{200} (kpc)	V_{200} (km/s)	$\log \rho_0$ $\left(\frac{M_\odot}{pc^3}\right)$	$\log h$ (pc)	χ^2_R
UGC05750	10.22 ± 0.65	8.44 ± 2.7	88 ± 9.2	64 ± 7	-2.19	3.94	0.25
UGC05764	41.17 ± 0.29	0.79 ± 0	40 ± 0.2	29 ± 0	-0.63	2.99	2.44
UGC05829	16.54 ± 1.06	2.55 ± 0.4	59.1 ± 3.4	43 ± 3	-1.67	3.55	0.18
UGC05918	24.38 ± 1.86	0.61 ± 0.1	36.6 ± 1.9	27 ± 1	-1.23	3.18	0.04
UGC05986	28.52 ± 0.17	11.36 ± 0.2	97.2 ± 0.6	71 ± 0	-1.06	3.53	1.71
UGC05999	13.35 ± 0.83	12.69 ± 2	100.8 ± 5.2	74 ± 4	-1.90	3.88	0.76
UGC06399	21.84 ± 1.02	6.13 ± 0.8	79.1 ± 3.3	58 ± 2	-1.36	3.56	0.06
UGC06446	32.33 ± 1.28	3.05 ± 0.2	62.7 ± 1.4	46 ± 1	-0.91	3.29	0.54
UGC06667	24.69 ± 0.48	5.57 ± 0.4	76.6 ± 1.6	56 ± 1	-1.22	3.49	0.09
UGC06917	25.82 ± 0.49	7.54 ± 0.4	84.7 ± 1.5	62 ± 1	-1.17	3.52	0.25
UGC06923	22.64 ± 0.52	4.01 ± 0.4	68.6 ± 2.3	50 ± 2	-1.32	3.48	0.38
UGC06930	25.61 ± 1.24	7.47 ± 0.5	84.5 ± 1.8	62 ± 1	-1.18	3.52	0.18
UGC06983	31.18 ± 1.41	7.33 ± 0.4	83.9 ± 1.6	61 ± 1	-0.95	3.43	0.54
UGC07089	11.66 ± 0.69	10.21 ± 3.6	93.8 ± 10.1	68 ± 7	-2.05	3.91	0.08
UGC07125	13.51 ± 0.57	2.07 ± 0.1	55.1 ± 1	40 ± 1	-1.89	3.61	0.26
UGC07151	29.49 ± 1.27	1.7 ± 0.1	51.6 ± 0.9	38 ± 1	-1.02	3.24	1.3
UGC07261	33.17 ± 2.97	1.98 ± 0.4	54.2 ± 3.2	40 ± 2	-0.88	3.21	0.13
UGC07399	49.68 ± 0.6	3.92 ± 0.1	68.1 ± 0.5	50 ± 0	-0.41	3.14	1.3
UGC07524	19.68 ± 0.21	4.13 ± 0.1	69.3 ± 0.8	51 ± 1	-1.48	3.55	0.43
UGC07559	15.64 ± 1.84	0.54 ± 0.3	35.3 ± 7	26 ± 5	-1.73	3.35	0.17
UGC07603	31.8 ± 0.87	1.73 ± 0.1	51.9 ± 0.7	38 ± 1	-0.93	3.21	0.36
UGC07608	22.39 ± 1.89	3.67 ± 0.9	66.6 ± 5.9	49 ± 4	-1.33	3.47	0.07
UGC07690	52.12 ± 4.92	0.53 ± 0.1	34.9 ± 1.7	25 ± 1	-0.36	2.83	0.05
UGC07866	21.72 ± 3.3	0.23 ± 0.1	26.3 ± 3.7	19 ± 3	-1.36	3.08	0.05
UGC08286	32.49 ± 0.36	3.42 ± 0.1	65.1 ± 0.3	48 ± 0	-0.91	3.30	0.94
UGC08490	39.98 ± 1.06	2.62 ± 0.1	59.6 ± 0.8	44 ± 1	-0.67	3.17	0.56
UGC08550	29.87 ± 0.71	1.15 ± 0.1	45.3 ± 0.7	33 ± 1	-1.00	3.18	0.74
UGC09037	7.46 ± 0.2	124.84 ± 33	216 ± 17.9	158 ± 13	-2.52	4.46	1.03
UGC10310	25.34 ± 2.28	2.32 ± 0.3	57.2 ± 2.6	42 ± 2	-1.19	3.35	0.13
UGC11455	13 ± 0.4	187 ± 14	247 ± 6	180 ± 4	-1.93	4.28	2.55
UGC11557	6.27 ± 1.21	1927 ± 858	537 ± 181	393 ± 132	-2.70	4.93	1
UGC11820	13.3 ± 0.26	6.48 ± 0.3	80.6 ± 1.1	59 ± 1	-1.91	3.78	10.49
UGC12506	32.9 ± 0.7	76.6 ± 1.3	184 ± 1	134 ± 1	-0.89	3.75	0.7
UGC12632	21.31 ± 0.76	2.89 ± 0.1	61.6 ± 0.8	45 ± 1	-1.39	3.46	0.08
UGC12732	19.1 ± 0.5	6.4 ± 0.3	80.2 ± 1.4	59 ± 1	-1.51	3.62	1.29
UGCA281	45.4 ± 2	0.12 ± 0	21.5 ± 1	16 ± 1	-0.52	2.68	0.13
UGCA442	19.2 ± 0.22	2.08 ± 0	55.2 ± 0.3	40 ± 0	-1.50	3.46	0.52
UGCA444	23.41 ± 0.88	0.33 ± 0	30 ± 1.1	22 ± 1	-1.28	3.11	0.23

[d]Best-fit parameter values, assuming a BURK profile. Columns as in Table A1.

REFERENCES

Abdurro'uf, Accetta, K., Aerts, C., et al. 2022, ApJS, 259, 35, https://doi.org/10.3847/1538-4365/ac4414

Aniyan, S., Freeman, K., Arnaboldi, M., et al. 2018, MNARAS, 476, 1909, https://doi.org/10.1093/mnras/sty310

Bell, E. F. & de Jong, R. S. 2001, ApJ, 550, 212, https://doi.org/10.1086/319728

Binney, J. & Tremaine, S. 1987, Galactic Dynamics, (Pincenton, NJ: PUP)

Blais-Ouellette, S., Amram, P., & Carignan, C. 2001, AJ, 121, 1952, https://doi.org/10.1086/319944

Bosma, A. 1978, The distribution and kinematics of neutral hydrogen in spiral galaxies of various morphological types, PhD. Thesis, Groningen Univ.

_____. 1981, AJ, 86, 1825, https://doi.org/10.1086/113063

Bruzual, G. & Charlot, S. 2003, MNRAS, 344, 1000, https://doi.org/10.1046/j.1365-8711.2003.06897.x

Burkert, A. 1995, AJ, 447, 25, https://doi.org/10.1086/309560

Cantó, J., Curiel, S., & Martínez-Gómez, E. 2009, A &A, 501, 1259, https://doi.org/10.1051/0004-6361/200911740

Carignan, C. & Freeman, K. C. 1985, ApJ, 294, 494, https://doi.org/10.1086/163316

Casertano, S. 1983, MNRAS, 203, 735, https://doi.org/10.1093/MNRAS/203.3.735

Cody, W. J. 1993, ACM Transactions on Mathematical Software, 19, 22, https://doi.org/10.1145/151271.151273

Curiel, S., Cantó, J., Georgiev, L., Chávez, C., & Poveda, A. 2011, A&A, 525, 78, https://doi.org/10.1051/0004-6361/201015693

de Blok, W. J. G. 2010, AdAsT, 2010, https://doi.org/10.1155/2010/789293

Freeman, K. C. 1970, ApJ, 160, 811, https://doi.org/10.1086/150474

Holland, J. H. et al. 1992, Adaptation in Natural and Artificial Systems. An Introductory Analysis with Applications to Biology, Control, and Artificial Intelligence, (Cambridge, MA: MIT Press)

Huchtmeier, W. & Richter, O.-G. 1989, A&A, 210, 1
Katz, H., Lelli, F., McGaugh, S. S.,et al. 2017, MNRAS, 466, 1648, https://doi.org/10.1093/mnras/stw3101
Kennicutt, R. C. Jr., Armus, L., Bendo, G., et al. 2003, PASP, 115, 928, https://doi.org/10.1086/376941
Kent, S. M. 1986, AJ, 91, 1301, https://doi.org/10.1086/114106
Korsaga, M., Epinat, B., Amram, P., et al. 2019, MNRAS, 490, 2977, https://doi.org/10.1093/mnras/stz2678
Kroupa, P. & Jerabkova, T. 2021, arXiv:2112.10788, https://doi.org/10.48550/arXiv.2112.10788
Kuzio de Naray, R., McGaugh, S. S., & de Blok, W. J. G. 2008, ApJ, 676, 920, https://doi.org/10.1086/527543
Lelli, F., McGaugh, S. S., & Schombert, J. M. 2016a, ApJ, 816, 14, https://doi.org/10.3847/2041-8205/816/1/L14
_____. 2016b, AJ, 152, 157, https://doi.org/10.3847/0004-6256/152/6/157
Leroy, A. K., Walter, F., Brinks, E., et al. 2008, AJ, 136, 2782, https://doi.org/10.1088/0004-6256/136/6/2782
Li, P., Lelli, F., McGaugh, S., & Schombert, J. 2020, ApJs, 247, 31, https://doi.org/10.3847/1538-4365/ab700e
Marchesini, D., D'Onghia, E., Chincarini, G., et al. 2002, ApJ. 575, 801, https://doi.org/10.1086/341475
McGaugh, S. S., Rubin, V. C., & De Blok, W.J.G. 2001, AJ, 122, 2381, https://doi.org/10.1086/323448
McGaugh, S. S. & Schombert, J. M. 2014, AJ, 148, 77, https://doi.org/10.1088/0004-6256/148/5/77
Meidt, S. E., Schinnerer, E., Van de Ven, G., et al. 2014, AJ, 788, 144, https://doi.org/10.1088/0004-637X/788/2/144
Meurer, A., Smith, C. P., Paprocki, M., et al. 2017, Peer J. Computer Science, 3, 103, https://doi.org/10.7717/peerj-cs.103
Milgrom, M. 1983, ApJ, 270, 365, https://doi.org/10.1086/161130
Navarro, J. F., Frenk, C. S., & White, S. D. M. 1997, ApJ, 490, 493, https://doi.org/10.1086/304888
Peebles, P. J. E. 2020, Cosmology's Century: An Inside History of our Modern Understanding of the Universe (Princeton, NJ: PUP)
Riess, A. G., Yuan, W., Macri, L. M., et al. 2022, ApJL, 934, 7, https://doi.org/10.3847/2041-8213/ac5c5b
Roberts, M. S. 1962, AJ, 67, 437, https://doi.org/10.1086/108752
Rodríguez-González, A., Esquivel, A., Raga, A., et al. 2012, AJ, 143, 60, https://doi.org/10.1088/0004-6256/143/3/60
Rubin, V. C., Ford, W. K. Jr., Strom, K. M., Strom, S. E., & Romanishin, W. 1978, ApJ, 224, 782, https://doi.org/10.1086/156426
Sackett, P. D. 1997, ApJ, 483, 103, https://doi.org/10.1086/304223
Schombert, J. & McGaugh, S. 2014, PASA, 31, 36, https://doi.org/10.1017/pasa.2014.32
Simon, J. D., Bolatto, A. D., Leroy, A., Blitz, L., & Gates, E. L. 2005, ApJ, 621, 757, https://doi.org/10.1086/427684
Sofue, Y. 2012, PASJ, 64, 75, https://doi.org/10.1093/pasj/64.4.75
_____. 2013, Planets, Stars and Stellar Systems Vol. 5, 985, https://doi.org/10.1007/978-94-007-5612-0_19
van Albada, T. & Sancisi, R. 1986, RSPTA, 320, 447, https://doi.org/10.1098/rsta.1986.0128
van Albada, T. S., Bahcall, J. N., Begeman, K., & Sancisi, R. 1985, ApJ, 295, 305, https://doi.org/10.1086/163375
Walker, M. G. & Penarrubia, J. 2011, ApJ, 742, 20, https://doi.org/10.1088/0004-637X/742/1/20

Ana M. Hidalgo-Gámez and Rodolfo de J. Zermeño: Escuela Superior de Física y Matemáticas, Instituto Politécnico Nacional, Unidad Profesional Adolfo López Mateos, Gustavo A. Madero, 07738, México, (amhidalgog@ipn.mx, rzermenop1800@alumno.ipn.mx).